Nucleic Acids Research, 2026, **54**, gkag165
https://doi.org/10.1093/nar/gkag165
Molecular and Structural Biology

Multisite phosphorylation of the AML-linked C-terminal of nucleophosmin (NPM1) orchestrates protein stability, DNA binding and charge block-driven phase separation

Pablo Rivero-García[1], Rafael L. Giner-Arroyo[1], Joaquín Tamargo-Azpilicueta[1], Abbey Telfer[2], Elisa Frezza[3], Adrián Velázquez-Campoy[4,5,6], Sofía Díaz-Moreno[2], Miguel A. De la Rosa[1], Irene Díaz-Moreno[1,*]

[1]Institute for Chemical Research—cicCartuja, University of Seville—CSIC, 41092 Seville, Spain
[2]Diamond Light Source—Harwell Science & Innovation Campus, OX11 0DE Didcot, United Kingdom
[3]Université Paris Cité, CiTCoM, CNRS, F-75006 Paris, France
[4]Institute for Biocomputation and Physics of Complex Systems (BIFI), and Department of Biochemistry and Molecular and Cell Biology, University of Zaragoza, 50018 Zaragoza, Spain
[5]Instituto de Investigación Sanitaria Aragón (IIS Aragón), 50009 Zaragoza, Spain
[6]Centro de Investigación Biomédica en Red en el Área Temática de Enfermedades Hepáticas y Digestivas (CIBERehd), 28029 Madrid, Spain
*To whom correspondence should be addressed. Email: idiazmoreno@us.es

Abstract

Nucleophosmin (NPM1) is a nucleolar protein commonly mutated in ∼30% of newly diagnosed acute myeloid leukemia (AML) cases. These mutations occur in the terminal exon of the NPM1 gene, affecting the C-terminal DNA-binding domain of the protein and causing its delocalization to the cytoplasm—a hallmark of NPM1-mutated AML. NPM1 shuttling to the nucleoplasm is tightly regulated by posttranslational modifications, such as phosphorylation of Ser254, Ser260, and Tyr271 of the DNA-binding domain. However, the structural mechanisms underlying this process remain unclear. In this work, we show that Ser-to-Asp (S254D–S260D) and Tyr-to-*p*CMF (*para*-carboxymethyl phenylalanine) (Y271*p*CMF) phosphomimetic mutations induce significant structural and dynamical rearrangements, as well as drastic modifications in electrostatic surface potential. These changes compromise recognition of a G-quadruplex sequence from the *c*-MYC promoter by reducing DNA-binding affinity, reshape histone capturing dynamics, and fade charge segregation in the histone-binding domain. Combination of such substitutions in a triple phosphomimetic variant (S254D–S260D–Y271*p*CMF) further destabilizes the domain's structure and triggers protein aggregation. Altogether, these findings suggest that phosphorylation of Ser254, Ser260, and Tyr271 of the C-end DNA-binding domain weakens both DNA affinity and charge block-driven liquid–liquid phase separation, offering a molecular explanation for the delocalization of NPM1 outside of the nucleolus.

Graphical abstract

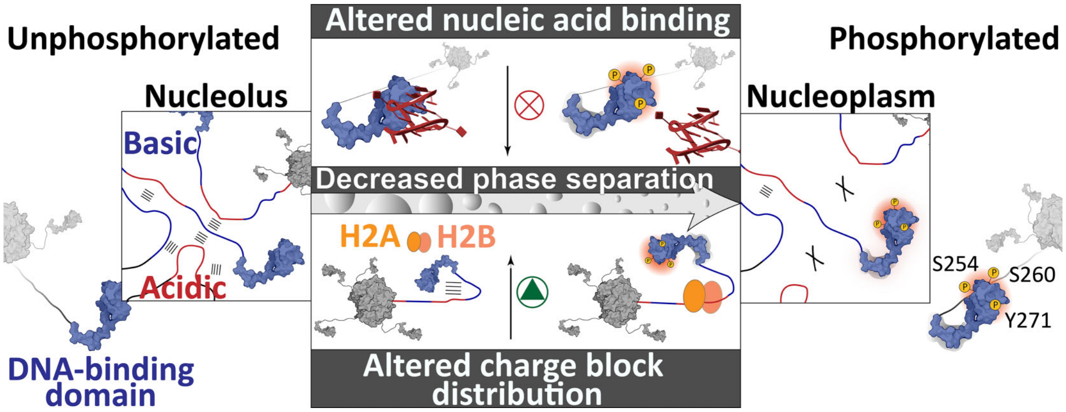

Received: July 23, 2025. **Revised:** January 12, 2026. **Accepted:** January 23, 2026

Introduction

Acute myeloid leukemia (AML) is an hematological disorder characterized by the abnormal proliferation and differentiation of a clonal population of myeloid stem cells [1]. The serial acquisition of somatic mutations in cells with the capacity to self-renew and propagate the neoplastic clone is crucial for leukemia development [2]. Advances in genetically based diagnosis have enabled the classification of AML into different subentities based on the presence or absence of clinically relevant cytogenetic and molecular abnormalities [3]. Among these, the 2022 World Health Organization classification on myeloid neoplasms has recognized nucleophosmin (NPM1)-mutated AML as a distinct entity, defined by this specific genetic abnormality regardless of blast counts [4]. Notably, NPM1 is involved in ribosome biogenesis, centrosome duplication, protein chaperoning [5], and cell proliferation [6]. It is prevalently mutated in approximately one-third of all diagnosed AML cases [7–11]. These mutations represent the most prominent class II mutations, according to the two-hit leukemogenesis model [1].

Most NPM1 leukemogenic mutations result in frameshift events that disrupt the C-terminal nucleic acid-binding domain. Structurally, the C-end domain of NPM1 consists of a three-helix bundle [12] (residues 241–294) and is connected to the N-terminal oligomerization domain (OD) through an intrinsically disordered region (IDR) [13] (Fig. 1A). This bundle, together with a short segment of the IDR (residues 224–241), constitutes the NPM1 DNA-binding domain (DBD; Fig. 1A and B), which binds DNA-based G-quadruplexes with high affinity, including the sequence found at the *c-MYC* oncogene promoter [14]. Frameshift mutations in this region result in the loss of the protein's nucleolar localization signal (NoLS), specifically the key residues Trp288 and Trp290 (Fig. 1B). This alteration leads to the formation of a new nuclear export signal, preventing proper incorporation of NPM1 into the nucleolus and promoting its mislocalization to the cytoplasm [15–17]. This mislocalization disrupts the cellular localization of NPM1, which is a critical hallmark in cancer development [18]. Due to its central role in nucleolar morphology and function, as well as in other extranucleolar processes, NPM1—and specifically its DBD—serves as a hub for post-translational modifications [19–21]. Notably, dual phosphorylation at Ser254 and Ser260 within the C-terminal DBD of NPM1 induces translocation from the nucleolus to the nucleoplasm [22]. Moreover, phosphorylation at Tyr271 under genotoxic stress has been associated with premature and extensive nucleolus-to-nucleoplasm translocation of NPM1 [20]. However, it remains unclear how dual phosphorylation at Ser254 and Ser260, phosphorylation at Tyr271 alone, or the combined modification at all three sites influences the structural architecture of the domain, its nucleic acid binding capacity, and overall protein dynamics.

In this study, we demonstrate that phosphomimetic mutations—Ser to Asp (S254D–S260D) and Tyr to *p*CMF (*para*-carboxymethyl phenylalanine) (Y271*p*CMF)—in the NPM1 DBD preserve the overall folding of the domain, despite inducing structural and dynamical rearrangements. These mutations markedly reshape the ESPs, leading to reduced DNA-binding affinity—as reflected by impaired recognition of a G-quadruplex sequence from the *c*-MYC gene promoter—along with diminished histone-capturing activity and a partial loss of charge segregation within the histone-binding domain. The combination of these substitutions in a triple phosphomimetic variant (S254D–S260D–Y271*p*CMF) further destabilizes the domain structure and leads to aggregation of the domain. Collectively, these findings suggest that phosphorylation at Ser254, Ser260, and Tyr271 could contribute to NPM1 delocalization outside of the nucleolus by compromising both DNA affinity and the propensity for charge block-based liquid–liquid phase separation (LLPS).

Materials and methods

DNA constructs

For protein expression, the coding sequence of C-end (C70) or full-length (FL) NPM1 fused with an N-terminal His-tag and inserted in pET28(+) bacterial expression vector was already available at our group [23]. NPM1 C70 and FL phosphomimetic variants were obtained via mutagenic polymerase chain reaction using the following primers: (i) 5′ GATATAGAAAAAGGTGGTGATCTTCCCAAAGTGGAAGCCAA 3′ and 5′ ATCACCACCTTTTTCTATATCTGCTTGCATTTTTGCTTTAATGT 3′ for the substitution of Ser254 and Ser260 codons for aspartate ones; and (ii) 5′ CAATTAGGTGAAGAATTGCTTCCGGATGACTGAC 3′ and 5′ CACCTAATTGATGAATTTGGCTTCCACTTTGGGA 3′ for the substitution of Tyr271 codon for an Amber STOP codon. The results were checked by Sanger Sequencing (Eurofins Genomics). G-quadruplex oligonucleotide Pu24I [24] of sequence 5′ TGAGGGTGGIGAGGGTGGGGAAGG 3′ was purchased from Sigma–Aldrich. The lyophilized Pu24I stock was resuspended in 20 mM sodium phosphate buffer (pH 7.2) and 100 mM KCl. For the G-quadruplex formation annealing, Pu24I was heated to 95°C for 15 min and left to cool down at room temperature overnight [24].

Protein expression and purification

pET28a(+) plasmid coding for NPM1 C70 or FL constructs were used to transform *Escherichia coli* BL21(DE3) cells via heat shock. Transformed cells were plated in lysogeny broth (LB)–agar solid media supplemented with 50 μg ml^{-1} kanamycin at 37°C. For protein expression of NPM1 C70 or FL WT and S254D–S260D, cells were grown at 37°C with shaking overnight on liquid LB medium supplemented with 50 μg ml^{-1} kanamycin, which was then used to inoculate 1.5 l cultures in 3 l flasks (1:10 dilution). Protein expression was induced once OD$_{600}$ reached a value of 0.8, adding isopropyl-β-D-thiogalactoside (IPTG) at 1 mM, and incubating for 20 h at 30°C with shaking.

To incorporate *p*CMF in position 271 of NPM1 C70 or FL, we followed previous protocols reported in the literature [25]. For the expression of NPM1 C70 or FL Y271*p*CMF, cells were cotransformed with the protein-coding pET28a(+) vector and the pEVOL plasmid. pEVOL encodes an aminoacyl transfer RNA (tRNA) synthetase/tRNA pair, specific for *p*CMF incorporation to the polypeptide chain upon recognition of the Amber (UAG) STOP codon. Transformed cells were cultured in LB supplemented with 50 μg ml^{-1} kanamycin and 20 μg ml^{-1} chloramphenicol and grown overnight at 37°C with shaking. These cells were used to inoculate 50 ml of fresh LB medium with a 1:10 dilution factor. Once OD$_{600}$ reached a value of 0.4, pEVOL expression was induced by adding arabinose at 0.02% (w/v) final concentration to the culture media. After a

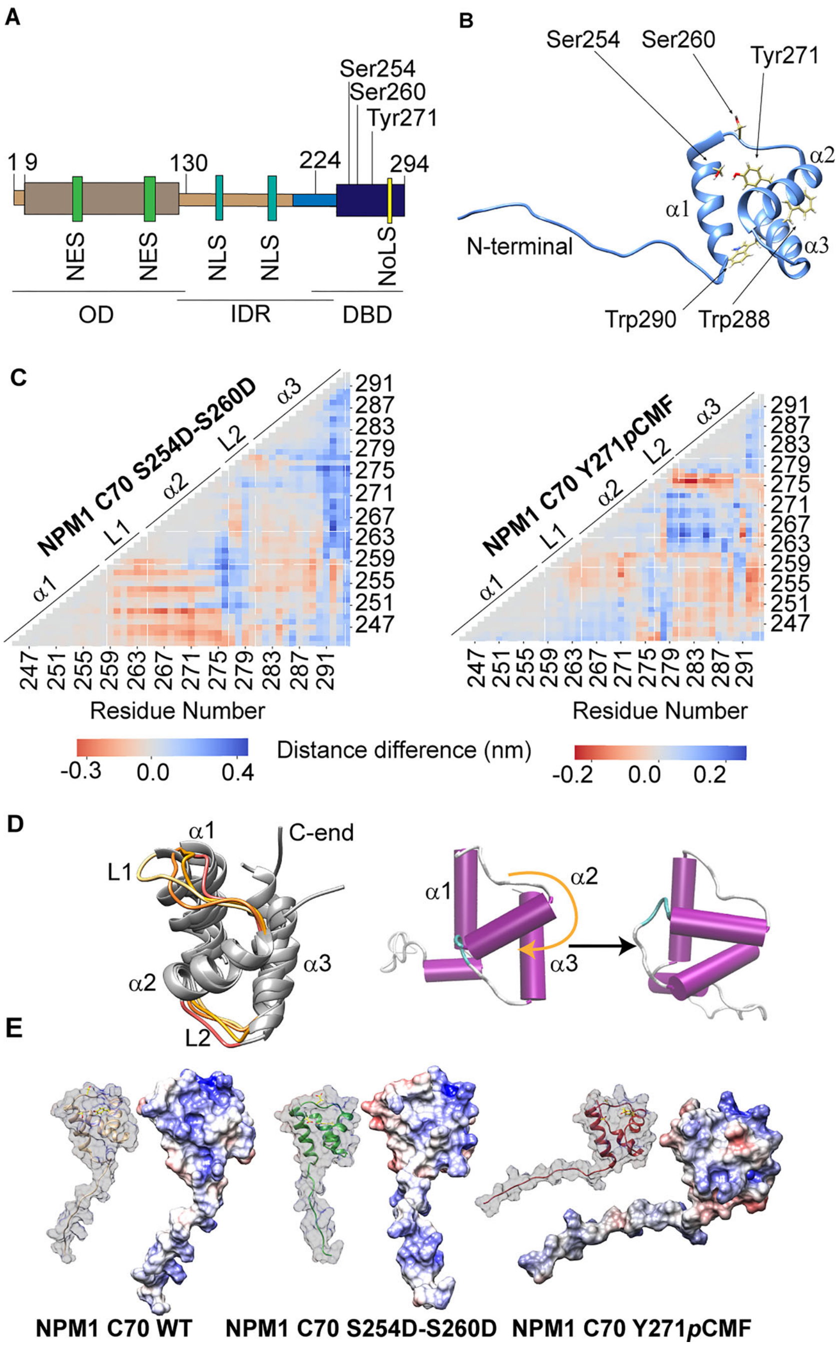

Figure 1. *In silico* molecular dynamics calculations of NPM1 C70 phosphomimetic variants. (**A**) Domain organization of NPM1. NES: nuclear export signal. NLS: nuclear localization signal. NoLS: nucleolar localization signal. OD: oligomerization domain. IDR: intrinsically disordered region. DBD: DNA-binding domain. The C-terminal basic stretch is highlighted in light blue. (**B**) Ribbon structure of the NPM1 C-terminal nucleic acid-binding domain. Phosphorylatable residues and Trp residues forming the NoLS are shown. (**C**) Mean distance difference heatmap of all residue pairs in the three-helix bundle of NPM1 C70 S254D-S260D (left) and NPM1 C70 Y271*p*CMF (right) with respect to NPM1 C70 WT. Mean distances were computed using sampled frames from two independent replicates for each variant. Residue pairs that distance from each other are colored blue, while those that become closer are colored red. (**D**) Representation of helix rearrangement in NPM1 C70 phosphomimetic variants. Left, NPM1 C70 S254D–S260D MD simulation frames aligned through α2. A color gradient from yellow to red indicates the progression of loop movements over time, illustrating helix rotation. Right, schematic representation of MD simulation frames showing α2 rotation in the NPM1 C70 Y271*p*CMF variant. (**E**) Electrostatic surface potential (ESP) comparison between MD frames of NPM1 C70 WT and phosphomimetic variants. Reference ribbon structures are depicted. The scale ranges from −5 (red) to +5 (blue) $K_B\ T/e$.

2-h incubation period, cells were collected at 3500 × *g* for 5 min and used to inoculate 250 ml of M9 minimal media in 1 l flasks. Upon reaching an OD_{600} of 0.8, the noncanonical amino acid *p*CMF was added at 1 mM and the expression of both plasmids was induced by adding 0.02% arabinose, 1 mM IPTG. Cultures were incubated at 30°C with shaking for 20 h.

^{15}N-labeled NPM1 C70 WT and S254D–S260D protein samples for Nuclear Magnetic Resonance (NMR) experiments were expressed in M9 minimal media, using 1 g l^{-1} $^{15}NH_4Cl$ as nitrogen source. Cells were grown at 37°C overnight in liquid LB media supplemented with 50 μg ml^{-1} kanamycin, collected and used to inoculate fresh M9 media. Protein expression was induced with 1 mM IPTG upon reaching an OD_{600} of 0.8. Cultures were grown for 20 h at 30°C with shaking. NPM1 C70 Y271*p*CMF expression was achieved as described above, using 1 g l^{-1} $^{15}NH_4Cl$ as nitrogen source.

Cells were collected at 4500 × *g* for 10 min at 4°C and resuspended in a lysis buffer composed by 20 mM Tris–HCl (pH 8.0), 800 mM NaCl, 10 mM Imidazole, 1 mM phenylmethylsulfonyl fluoride (PMSF), 500 μl cOmplete™ ethylenediaminetetraacetic acid (EDTA)-free Protease Inhibitor Cocktail (Roche) from a tablet per ml stock, 0.2 mg ml^{-1} lysozyme, 0.02 mg ml^{-1} DNase I (Roche), and 5 mM dithiothreitol (DTT). The cell extract was sonicated for 5 min and centrifuged at 27 000 × *g* for 30 min at 4°C to remove cell debris. Protein purification was carried out by affinity chromatography in a column with Ni-Sepharose (HisPur™ Ni-NTA Resin, Thermo Scientific™) previously equilibrated with lysis buffer.

Protein was eluted using a 10–300 mM imidazole step gradient. Protein-containing elution fractions were dialyzed in 20 mM sodium phosphate buffer (pH 7.2) and concentrated in Amicon® Ultra-15 Centrifugal Filter Units (3 kDa cutoff) until reaching the required concentration. Sample purity and protein integrity was assessed by sodium dodecyl sulfate–polyacrylamide gel electrophoresis (SDS–PAGE) and protein concentration was quantified through Bradford protein assay for NPM1 FL species or registering sample absorbance at 280 nm for NPM1 C70 species.

H2A and H2B expression was carried out similarly as described in [26]. Transformed *E. coli* BL21(DE3) were grown in LB liquid media. Once OD_{600} reached ∼0.6, 1 mM IPTG was added. Cells were collected after incubation for 3 h at 37°C. For inclusion bodies purification, collected cells were lysed in buffer containing 20 mM HEPES (pH 7.5), 300 mM NaCl, 30 mM imidazole, 1 mM DTT, 5% glycerol, cOmplete™ (Roche), 0.01% PMSF, 0.2 mg ml^{-1} lysozyme, and 0.2 mg ml^{-1}.DNase I (Roche). Resuspended cells were sonicated for 7 min. The resulting extract was centrifuged at 26 000 × *g* for 20 min at 4°C.

The pellet was resuspended in buffer containing 20 mM HEPES (pH 7.5), 200 mM NaCl, 1 mM EDTA, 1 mM DTT, 1% triton X-100, cOmplete™, 0.01% PMSF, 0.2 mg ml^{-1} lysozyme, and 0.2 mg ml^{-1} DNase I, using a douncer. The homogenized lysate was then centrifuged at 18 000 × *g* for 20 min. This process was repeated twice, and another two times using the same buffer without triton X-100, with a final centrifugation step at 22 000 × *g* for 30 min at 4°C. The remaining pellet was flash frozen in liquid nitrogen and stored at −20°C.

Inclusion bodies were solubilized in dimethyl sulfoxide, and later incubated in agitation for 1 h at room temperature in buffer containing 20 mM Tris–HCl (pH 7.5), 6 M guanidinium chloride, 1 mM DTT. The sample was then centrifuged at 23 000 × *g* for 30 min at 4°C. The supernatant was dialyzed against buffer containing 20 mM sodium acetate (pH 5.2), 7 M urea, 1 mM EDTA, 1 mM DTT, 200 mM NaCl at 4°C. The sample was loaded on a DAE cellulose column to eliminate residual DNA. Flowthrough was then loaded on a DEAE cellulose matrix for cation exchange chromatography. Elution was done using a 0.2–1 M NaCl step gradient. Samples were dialyzed against water with 1 mM DTT at 4°C and lyophilized afterward.

Histone dimer assembly

Lyophilized H2A and H2B were separately dissolved in buffer containing 20 mM Tris–HCl (pH 7.5), 6 M guanidinium chloride, 5 mM DTT. Protein concentration was determined using 280 nm absorbance. H2A and H2B were equimolarly mixed and dialyzed extensively in buffer containing 10 mM Tris–HCl (pH 7.5), 1 mM EDTA, 2 mM DTT, 2 M NaCl. To separate the dimers, the sample was loaded on a Superdex® 75 Increase (GE Healthcare) size exclusion chromatography column.

MALDI–MS and tryptic digestion

Pure NPM1 C70 and FL samples were run on a 15% and 10% SDS–PAGE, respectively. Coomassie-stained SDS–PAGE gel bands were cut and unstained using an NH_4CO_3 and acetonitrile solution. They were also treated with DTT to break disulfide bonding and with iodoacetamide for cysteine carbamidomethylation. Tryptic digestion was done using a 1:10 mix of bovine trypsin:substrate and overnight incubation at 37°C. After acetonitrile extraction, samples were acidified, desalted, and concentrated. Spectra were registered using an Ultraflextreme MALDI–TOF spectrometer (Bruker), available at the Biomolecular Mass Spectrometry Service in Pablo de Olavide University. The information given by the fingerprint spectra was compared with the results expected from the theorical digestion of the peptide, which included posttranslational modifications, cysteine carbamidomethylation, and methionine oxidation.

Molecular dynamics simulations

Molecular dynamics (MD) simulations were carried out using AMBER 14SB force field [27] in explicit solvent using OPC water models under periodic boundary conditions using an orthorhombic cell geometry, with a minimal distance between protein and cell walls of 10 Å. The net charge of the system was neutralized including chlorine and sodium atoms. Charges and force-field parameters for the *p*CMF residue were obtained from previous *ab initio* GAMESS calculations [25]. Charges and force-field parameters for the phosphoserine and phosphotyrosine with unprotonated phosphate group were retrieved from the AMBER Parameter Database [28]. The NMR-resolved structure of NPM1 C70 (PDB accession number: 2LLH [24]) was used as the starting structure of WT NPM1 C70 simulations, and as a template to generate the modified phosphomimetic and phosphorylated variants. Coordinates and topology parameters were obtained using AMBER's LeaP module.

MD simulations in equilibrium were performed using OpenMM [29] v7.4.2. Each system was subjected to 2 μs MD simulations at 298 K at a constant pressure of 1 atm after

2500 steps of energy minimization, using particle mesh Ewald (PME) electrostatics with an Ewald summation cut-off of 9 Å to account for Coulomb and van der Waals interactions. Replicates ($n = 2$) were run using the same initial coordinates and topology parameters. The simulation's trajectory statistics were analyzed using the CPPTRAJ [30] module of AMBER. The Mdtraj [31] Python module was used to compute the distance between residue pairs from two replicate simulations for each system, with the same starting coordinates, using the "closest heavy" method.

Replica exchange with solute tempering (REST2) simulations [32] were performed in GROMACS (v2023.5) [33] patched with plumed (v2.9.0) [34]. AMBER topology and coordinate files were converted to GROMACS-compatible format using *parmed* [35], and chlorine and sodium atoms were added to match a 150 mM ionic strength. The system was minimized using the steepest descent algorithm applying gradually decreasing isotropic force constants restraints (1000, 500, 250, 100, 50, 10 kJ mol^{-1} nm^{-2}) to the protein atoms, followed by an unrestrained minimization. The system was equilibrated for 20 ns at 300 K, using a velocity rescale thermostat and an isotropic pressure of 1 bar maintained using a C-rescale barostat, using PME with a cutoff of 11 Å for Coulomb and 9–11 Å for van der Waals interactions, and restricting the bond length using LINCS algorithm. To set the simulations, the charge, Lennard–Jones parameter, and proper dihedral potentials defined in the topology file were rescaled as described by a λ factor defined as

$$\lambda = \frac{T_{\min}}{T_i}, \qquad (1)$$

where $T_{\min}$ is the minimum temperature ($T = 280$ K for $\lambda = 0$) and T_i is the temperature of the ith replica [36]. The replica temperatures, T_i, were distributed following an exponential geometric progression,

$$T_i = T_{\min} \cdot \exp\left\{ i \cdot \frac{\log\left(\frac{T_{\max}}{T_{\min}}\right)}{n-1} \right\}, \qquad (2)$$

where $T_{\max}$ is the maximum temperature (550 K), and n is the number of replicas (24). Exchanges were attempted every 500 steps using the -hrex and -replex 500 options. The simulation length was at least 200 ns with a 2 fs timestep under periodic boundary conditions. Temperature and pressure were controlled using the v-rescale thermostat ($\tau = 0.1$ ps) and the Parrinello–Rahman barostat ($\tau = 0.5$ ps, 1 bar). Long-range electrostatics were treated using the PME method with a real-space cutoff of 11 Å, and van der Waals interactions were smoothly switched to zero between 9 and 11 Å. Hydrogen bonds were constrained using the LINCS algorithm. GPU acceleration was employed for nonbonded, PME, and bonded interactions, while position updates were handled on CPUs. To analyze the simulations, first we computed the effective temperature, T_{eff}, using the following equation [37]:

$$\langle T_{\text{eff}} \rangle = T_i \left(1 + \left(\sqrt{\frac{T_{\min}}{T_i}} - 1 \right) \left\langle \frac{E_{pw}\left(\vec{X}\right)}{E_{pp}\left(\vec{X}\right) + E_{pw}\left(\vec{X}\right)} \right\rangle \right), \qquad (3)$$

where $E_{pp}(\vec{X})$, $E_{pw}(\vec{X})$ designate protein–protein and protein–water potential energies, and T_i is the instantaneous temperature at the ith step.

To evaluate the evolution of the structure along the different repeats, we computed the backbone root mean square deviation (RMSD) for the folded region (residues 20–70) over the last half of the trajectories using "`gmx rms`" from the GROMACS suite, with the starting structure after equilibration as the reference. A conformation was defined as folded if its RMSD was below 2.5 Å, allowing us to estimate the fraction of folded states.

AM1BCC tool [38] of the Antechamber package, included in USCF Chimera v1.17 [39], was used to compute atom charges, and adaptive Poisson–Boltzmann solver [40] to calculate ESPs of NPM1 C70 variants. USCF Chimera v1.17 and VMD v1.9.4 [41] were used for simulation analysis and depiction.

Circular dichroism

Circular dichroism (CD) spectra of NPM1 C70 samples were registered in the far-UV range (190–250 nm) at 298 K in 20 mM sodium phosphate (pH 7.2) buffer. For each sample, 20 scans were averaged in a Jasco J-815 spectropolarimeter equipped with a Peltier temperature-control system, using a 1-mm quartz cuvette. Protein concentration was 15 µM. Far-UV CD spectra of NPM1 FL samples were registered in 10 mM sodium phosphate (pH 7.4) buffer with the same system setup. Protein concentration was 1 µM of the pentameric form.

For far-UV (195–250 nm) CD temperature ramp measurements of NPM1 C70 WT and S254D–S260D–Y271*p*CMF variant, four scans were averaged in 1°C increments using a 10-mm quartz cuvette. Samples were prepared in 20 mM sodium phosphate (pH 7.2) buffer at 2.5 µM protein concentration. The stability parameters for the protein were estimated by nonlinear regression data analysis applying the single transition model in which the unfolding Gibbs energy, ΔG, is given by:

$$\Delta G\,(T) = \Delta H\,(T_{\text{m}}) \left(1 - \frac{T}{T_{\text{m}}}\right) + \Delta C_P \left(T - T_m - T\ln\frac{T}{T_m}\right)$$

$$\langle S \rangle = \frac{S_N + S_U \exp(-\Delta G(T)/\text{RT})}{1 + \exp(-\Delta G(T)/\text{RT})},$$

where ΔH is the unfolding enthalpy, T_{m} is the unfolding temperature, ΔCP is the unfolding heat capacity, $\langle S \rangle$ is the measured signal at each temperature, S_N and $S_U$are the intrinsic signals for the native and the unfolded states, which are considered linear functions of the temperature. The populations of the native and unfolded states, P_N and P_U, are related to the unfolding Gibbs energy:

$$P_N\,(T) = \frac{1}{1 + \exp(-\Delta G(T)/\text{RT})},$$

$$P_U\,(T) = \frac{\exp(-\Delta G(T)/\text{RT})}{1 = \exp(-\Delta G(T)/\text{RT})}.$$

NMR measurements

1D ^{1}H, 2D [^{1}H, ^{15}N] HSQC, 3D NOESY-HSQC, and 3D TOCSY-HSQC NMR spectra of all NPM1 C70 variants were acquired on a Bruker Avance III 500 MHz system at 298 K (unless otherwise specified). Structural characterization experiments were carried out in 20 mM sodium phosphate buffer (pH 7.2) supplemented with tris(2-carboxyethyl)phosphine (TCEP) reducing agent at 5 equivalents of the protein molar concentration. All samples contained 5% D_2O for the adjustment of the lock signal. For 1D experiments protein concentrations ranged 80–300 µM, whereas 2D spectra were performed at 500 µM. 3D TOCSY-HSQC and NOESY-HSQC spectra were acquired at higher protein concentration, ranging 500–900 µM.

Titration experiments were performed in 20 mM sodium phosphate (pH 7.2) supplemented with 5 equivalents of TCEP and 100 mM KCl. 2D [^{1}H, ^{15}N] HSQC spectra of 50 µM NPM1 C70 were recorded in the absence and in the presence of 50 µM nonlabeled Pu24I oligonucleotide (1:0 and 1:1 molar ratio). For the assignment of NPM1 C70 phosphomimetic variants, 3D TOCSY-HSQC and NOESY-HSQC spectra were acquired. Supplementary Fig. S1 shows the 2D [^{1}H, ^{15}N] HSQC spectra with assigned backbone amide resonances. Amide backbone resonance assignments are available at the Biological Magnetic Resonance Data Bank (BMRB accession numbers 52438 and 52439). Acquisition parameters used in 2D and 3D NMR experiments are included in Supplementary Table S1.

TopSpin v4.2.0 software was used for the initial steps of spectra processing. For the assignment of backbone resonances and chemical-shift perturbations (CSPs) calculations, POKY NMR [42] software was used.

Isothermal titration calorimetry measurements

To study the interaction between NPM1 C70 phosphomimetic variants and Pu24I oligonucleotide, isothermal titration calorimetry (ITC) measurements were performed using a Nano ITC Low Volume (TA Instruments, USA) at 298 K. Experiments consisted of 17 successive 2.9 µl injections of a 300 µM NPM1 C70 solution into the cell, which contained a 20 µM solution of Pu24I oligonucleotide. Samples were prepared in a 20 mM sodium phosphate (pH 7.2), 100 mM KCl, 1.5 mM TCEP buffer. The delay between injections was set to 150 s to allow for baseline recovery and steering was maintained constant at 300 rpm during the acquisition. All samples were degassed prior to the experiments. To determine the binding affinity (dissociation constant, K_D, and binding Gibbs energy, ΔG) and the enthalpic and entropic contributions (ΔH and $-T\Delta S$), the experimental data were analyzed considering an interaction model of a single binding site using user defined routines in Origin 7.0 (OriginLab Corp.) software.

Histone-capture disaggregation assay

Histone-capture disaggregation assays were done similarly as described by Lorton *et al.* [43]. To form histone–DNA aggregates, H2A/H2B dimers were mixed with a 500-bp DNA fragment in a 15:1 molar ratio (300 nM histones and 20 nM DNA) in a 20 µl reaction volume in buffer containing 25 mM sodium phosphate (pH 7.0), 150 mM NaCl, and 1 mM EDTA. After incubating at 23°C for 15 min, NPM1 FL WT or phosphomimetic species were added to the mix at the monomeric NPM1: H2A/H2B dimer ratios shown. Samples were then incubated for another 30 min at 23°C. 2.8 µl of 50% glycerol were added to each sample and 10 µl of the mix were loaded on a 0.5% agarose Tris-borate-EDTA (TBE) gel. The electrophoresis was run for 45 min at 100 V and gels were post-stained using SYBR Gold nucleic acid stain (Thermo Scientific). Image analysis of the gels was done using ImageJ 1.54g [44]. DNA bands in each gel were quantified relative to their corresponding free DNA control. Intense bands near the wells of the gel were used to quantify aggregate DNA. Control experiments in the absence of H2A/H2B dimers were performed to ensure that the binding of NPM1 FL to DNA did not interfere with the assay. These assays were carried out at the highest chaperone concentration (4.8 µM of the monomeric form) for all NPM1 FL species.

Phase separation assays

Experiments were performed as previously described [45, 46]. Briefly, NPM1 FL species at a pentameric concentration ranging 0.25–10 µM were mixed with 13% Ficoll™ PM70 (Cytiva) molecular crowding agent in a 10 mM sodium phosphate buffer (pH 7.4) containing 150 mM NaCl. After mixing, samples were mounted in a glass slide and covered with a coverslip, kept together by a layer of pierced 3M™ double-sided, 100-µm-thick tape. Samples were incubated at room temperature for 10 min to allow the droplets to settle in the slide before image acquisition. Multiple microscopy field images (4–7) of two mounted samples were acquired for each experimental condition using a Leica CTR 6000 microscope. Image processing was performed with the LASX (Leica Microsystems) and FIJI (ImageJ) softwares [44]. FIJI's trainable Weka segmentation tool was employed for image segmentation and droplet area occupancy quantification. Pairwise comparisons of droplet area occupancy were done using a Mann-Whitney U test in Origin 7.0 (OriginLab Corp.) software.

Results

Molecular dynamics simulations on NPM1 C70 phosphomimetic variants suggest helix-bundle destabilization

To explore whether the delocalization of NPM1 triggered by phosphorylation in its DNA binding C-terminal domain [20, 22] correlates with changes in protein structure, dynamics, or nucleic acid binding, we analyzed phosphomimetic variants on an NPM1 construct that comprises its last 70 amino acids (NPM1 C70), since its kinases are still unknown. Ser254 and Ser260 were replaced by aspartates (NPM1 C70 S254D-S260D), while Tyr271 was substituted by the noncanonical amino acid *para*-carboxymethyl phenylalanine (*p*CMF) (NPM1 C70 Y271*p*CMF). The combination of the three substitutions was also tested (NPM1 C70 S254D-S260D-Y271*p*CMF).

During MD simulations on WT and the three NPM1 C70 phosphomimetic variants, radius of gyration (RoG) values remained constant and showed a similar degree of compactness among different variants (Supplementary Fig. S2A–C). RMSD values along the simulations remain approximately in a ±1 Å range for most replicates, while in some of them occasional fluctuations could be observed (Supplementary Fig. S2A–C). The convergence of RMSD and RoG values in the ns–µs timescale suggests the absence of global unfolding events in the domain.

Three α-helical tracts are clearly distinguished for the three variants in the secondary structure analyses of the trajectories (Supplementary Fig. S2A–C). Interestingly, while the Ser-to-Asp substitutions are located at the end of helix 1 (α1), a slight instability of helices 2 (α2) and 3 (α3) was detected during the trajectories. Similarly, while the Y271*p*CMF substitution takes place at α2, a decrease in the stability of α1 and α3 helices was observed. These observations were consistently reproduced, albeit with different degrees of destabilization. Altogether, these findings point to a broader effect of the phosphorylation events, spanning the entirety of the domain.

Difference in distances of all residue pairs in the three-helix bundle between phosphomimetic and WT NPM1 C70 species were computed (Fig. 1C). In the S254D–S260D and Y271*p*CMF variants, there is an approach between α1 and α3, while loop 2 (L2) separates from α1 and α2. In the NPM1 C70 S254D–S260D variant, α3 also distances from the end of α2 (before loop 2); while in NPM1 C70 Y271*p*CMF, α3 takes a tighter turn and converges closer toward the end of α2. It is worth noting that the C-end of α3 in NPM1 C70 S254D–S260D variant became unstable during simulations, which is reflected in the increased distance from the rest of the domain. Altogether, these findings indicate that slight structural rearrangements allow the accommodation of the substituted phosphomimetic residues (Fig. 1D).

The effect of mutations was further explored performing ESP calculations on both variants in comparison with the WT protein (Fig. 1E). ESPs were displayed using MD frames in which the IDR was mostly extended, and the three-helix bundle remained compact. The positively charged groove between α1 and α2 helices in NPM1 C70 WT harbors the binding surface of the G-quadruplex-forming DNA oligo Pu24I [24] and encompasses residues Ser254, Ser260, and Tyr271. Accordingly, the ESP of the C-end phosphomimetic NPM1 species (NPM1 C70 S254D–S260D or Y271*p*CMF) is substantially less positive in the two-helix interface and the adjacent unstructured N-terminal block (Fig. 1E), pointing toward an effect on the domain ability to establish electrostatic interactions with negatively charged molecules, such as nucleic acids.

Cotranslational incorporation of canonical and noncanonical phosphomimetic residues may result in only a partial analogy of phosphorylation, without fully reproducing the hydration layer, tetrahedral geometry, and formal charges of phosphate [47]. A workflow that combines computational and biochemical approaches to better decipher how phosphorylation events affect protein structure and function has been previously reported [48]. Therefore, to assess the extent to which Asp and noncanonical *p*CMF phosphomimetic substitutions recapitulate the structural and electrostatic effects of NPM1 phosphorylation at Ser254–Ser260 and Tyr271, we performed MD simulations on phosphorylated variants of the NPM1 C70 construct, modeled with deprotonated phosphate groups. Analysis of RMSD and RoG indicated structural stability across the simulation timescale (Supplementary Fig. S3A and B). The three-helix bundle secondary structure was preserved throughout the trajectories, though phosphorylated variants exhibited a higher degree of destabilization relative to their phosphomimetic counterparts (Supplementary Fig. S3A and B). Residue–residue distance mapping of the helical core revealed conserved dynamic patterns in the phosphorylated forms, occurring within a similar distance range as observed in the phosphomimetic variants (Supplementary Fig. S3D). As anticipated, ESP alterations were substantially more pronounced in the phosphorylated variants compared to the mimetics (Supplementary Fig. S3E), indicating a potentially greater influence on nucleic acid-binding affinity. Collectively, these MD simulations demonstrate that while phosphomimetic substitutions induce milder perturbations than *bona fide* phosphorylation, they nonetheless preserve key structural and electrostatic features, supporting their utility as proxies for studying NPM1 phosphorylation in contexts where the kinases remain unidentified.

Ser254–Ser260 and Tyr271 phosphomimetic substitutions result in mild domain-level perturbations

To validate the *in silico* predictions, we resorted to expressing, purifying, and biophysically characterizing NPM1 C70 WT, S254D–S260D, and Y271*p*CMF protein variants (Supplementary Fig. S4) [48]. After protein purification (Supplementary Fig. S4A), noncanonical amino acid *p*CMF incorporation and aspartate substitutions in the appropriate positions were confirmed by tandem mass spectrometry (MSMS) upon trypsin digestion of SDS–PAGE protein bands (Supplementary Fig. S4B and C).

Far UV–CD spectroscopy shows patterns consistent with an α-helical protein, with similar spectra between NPM1 C70 WT and phosphomimetic species (Supplementary Fig. S4D). Two-dimensional NMR [^{1}H, ^{15}N] heteronuclear single quantum coherence (^{15}N-HSQC) spectra of S254D–S260D and Y271*p*CMF NPM1 C70 species show disperse signals in the amide region, consistent with monomeric, well-folded conformations (Fig. 2A).

To gather information about the structural changes induced by the phosphomimetic modifications, 3D TOCSY-HSQC and 3D NOESY-HSQC NMR experiments were run for the assignment of protein backbone amide resonances of NPM1 C70 S254D–S260D and Y271*p*CMF species (BMRB accession numbers: 52439 and 52438, respectively). [^{1}H, ^{15}N]-HSQC displaying amide backbone resonances assignment are shown in Supplementary Fig. S1. Then, CSPs of protein backbone amide resonances comparing WT and phosphomimetic NPM1 C70 species were plotted (Fig. 2B) and displayed over NPM1 C70 MD simulations conformers (Fig. 2C). For the S254D–S260D variant, perturbations of eight amide resonances were overall significantly larger ($\Delta\delta_{avg} > \mu + 2\sigma$) than in the WT construct. Namely, Asp254 signal experienced the largest shift, followed by Met251 and Gln252. Other nearby residues located in α1, close to the mutation sites (Ile247, Lys248, Ala249, Lys250, Ala253, and Ile255), also shifted substantially. Moreover, resonances corresponding to residues in α2 (Val272) and α3 (Thr279 and Lys292) showed subtle but significant shifts ($\Delta\delta_{avg} > \mu + \sigma$). Altogether, these findings underline the tight connection within the three-helix bundle, in agreement with the long-range effect inferred by MD simulations. Amide resonance of Asp260 was hardly identified in the NPM1 C70 S254D–S260D spectrum and remained unassigned.

The magnitude of the CSPs of the Y271*p*CMF variant were smaller when compared to the ones calculated for NPM1 C70 S254D–S260D (Fig. 2B). However, six residues (Thr237, Ile255, Ser260, Val272, Cys275, and Phe276) underwent significant CSPs ($\Delta\delta_{avg} > \mu + 2\sigma$). Due to the usage of ^{15}N-unlabeled *p*CMF in the expression of NPM1 C70 Y271*p*CMF, this residue was not assigned. Still, residues in the surroundings experience significant CSPs (Val272, Cys275, Phe276). Interestingly, the CSP magnitude is almost equivalent between α1 and α2, which highlights the wide impact of this position on the NPM1 C70 structure, affecting not only residues

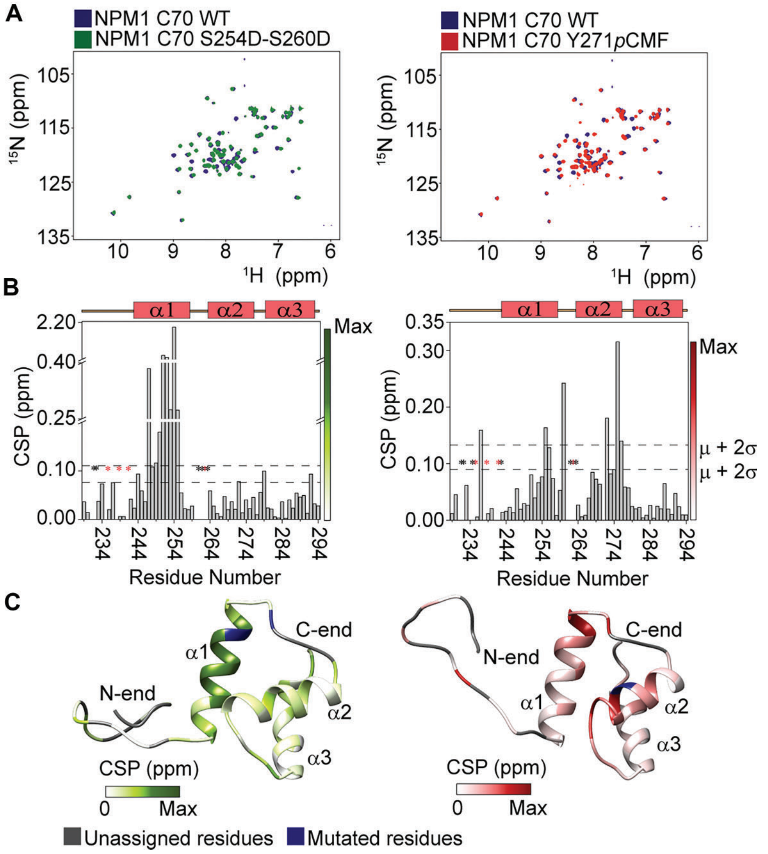

Figure 2. NMR structural characterization of NPM1 C70 phosphomimetic variants. (**A**) Superimposed ^{15}N-HSQC spectra of NPM1 C70 WT and phosphomimetic variants. (**B**) CSP differences (absolute values) of amide groups between NPM1 C70 WT and phosphomimetic variants. Mean CSPs plus 1–2 standard deviations are indicated in the plots. Asterisks denote unassigned signals, shown in gray. Prolines are marked with red asterisks. (**C**) CSP maps overlaid onto MD simulation frames of NPM1 C70 phosphomimetic variants. Left panels correspond to NPM1 C70 S254D–S260D, and right panels correspond to NPM1 C70 Y271*p*CMF.

adjacent to the mutation but also the ones located in the spatially opposing helix.

Interestingly, several resonances (including Ile255 or Val272) shifted substantially in the spectra of both phosphomimetic variants, suggesting a common effect of the different phosphorylations in the cavity formed in the interface of helices α1 and α2. The crosstalk among positions 254, 260, and 271 is also made clear by the remarkable shift that Ser260 experiences when Tyr271 is replaced in the *p*CMF271 variant.

NPM1 phosphomimetic variants display changes in binding to the *c-MYC* promoter DNA oligonucleotide Pu24I

NPM1 was initially thought to bind unspecifically to both RNA and DNA [13, 49]. However, current evidence shows preferential binding to G-quadruplex structured DNA molecules [14, 24, 50, 51] like the Pu24I oligonucleotide, derived from the *c-MYC* protooncogene promoter [14, 24]. This 24-bp oligonucleotide populates only one of the possible G-quadruplex structures thanks to a guanine to inosine substitution [52].

Based on the changes observed in the ESP of the phosphomimetic variants (Fig. 1E), we hypothesized that phosphorylations at Ser254, Ser260, and Tyr271 might decrease nucleic acid binding, favoring the escape of NPM1 from the nucleolus. To test this hypothesis, 2D [^{1}H, ^{15}N]-HSQC NMR titration experiments of ^{15}N-labeled NPM1 C70 species were recorded upon addition of an equimolar ratio of unlabeled Pu24I. CSPs of NPM1 C70 amide resonances were monitored to identify differential binding mode to Pu24I in the phosphomimetic variants (Fig. 3A) and were displayed over representative frames of the NPM1 C70 MD simulations (Fig. 3B).

Regarding CSP maps, α1 and α2 of NPM1 C70 WT were found to be involved in the interaction with DNA (Fig. 3B). For α1, the largest CSPs of the WT species are attributed to Lys248, Met251, Gln252, Ser254, and Ile255; except for Ile255, this was also the case in the NPM1 Y271*p*CMF species. On the contrary, NPM1 C70 S254D–S260D main CSPs involve Ile247, Gln252, Ala253, and Asp254. While the specific residues involved in the interaction vary between NPM1 C70 species, the stretch ranging from residues 244 to 255 in α1 is consistently involved in the interaction in all of them (Fig. 3A). In fact, CSPs corresponding to Val244 and Glu245—located at the start of α1—were among the highest ones in all variants. Regarding α2, the largest CSPs of NPM1 C70 WT correspond to Ile269 and Tyr271, one of the phosphorylation target positions analyzed in this work. In both phosphomimetic variants, Phe268, Ile269 and Cys275 are the residues that underwent the largest CSPs. Interestingly, in NPM1 C70 WT, eight residues broadened beyond detection: Phe268, Lys273, Cys275 (described to partake in the protein–oligo interface [24]), Phe276, and Thr279. The number of broadened signals was reduced to three in the

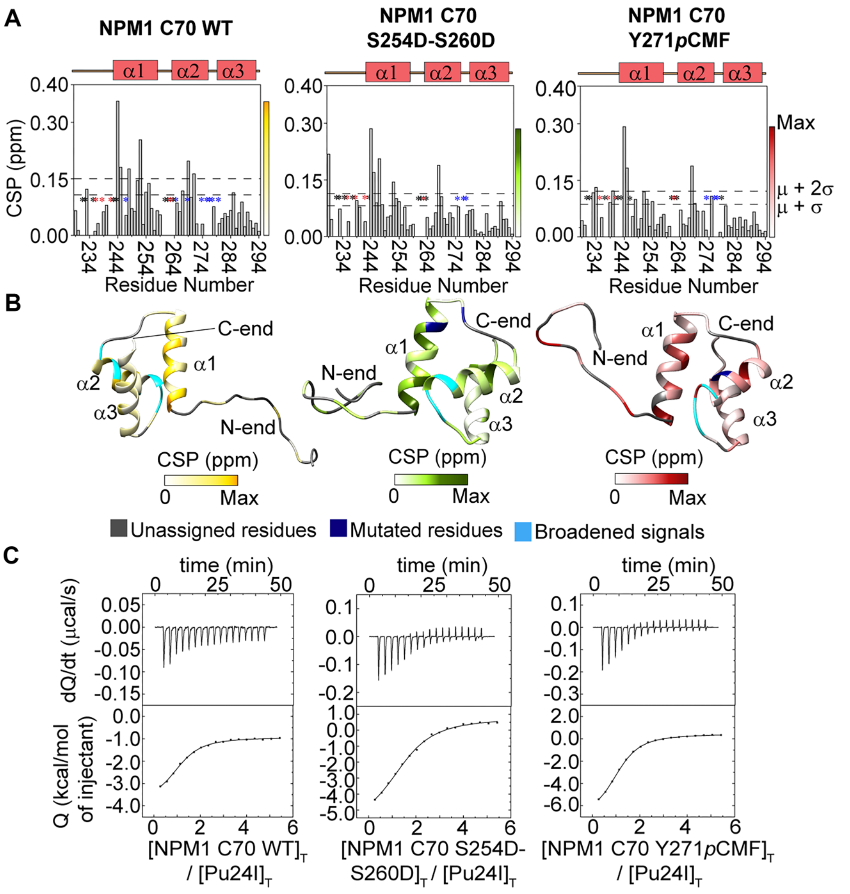

Figure 3. DNA binding of NPM1 C70 phosphomimetic variants. (**A**) Average CSPs of amide groups of NPM1 C70 WT and phosphomimetic variants in complex with the G-quadruplex *c*-myc promoter Pu24I at equimolar concentrations. Dashed lines represent mean CSP plus 1–2 standard deviations. Asterisks denote unassigned signals (gray), broadened signals (blue), and prolines (red). (**B**) CSP maps upon Pu24I binding for NPM1 C70 WT and phosphomimetic variants depicted over MD simulation frames. (**C**) ITC assays for NPM1 C70 WT and phosphomimetic variants with Pu24I. Thermograms (upper) and binding isotherms (lower) calculated for each interaction are shown. Left panels correspond to NPM1 C70 WT, middle panels to NPM1 C70 S254D-S260D, and right panels to NPM C70 Y271*p*CMF.

case of S254D–S260D (i.e. Lys273, Cys275, Phe276) and Y271*p*CMF (Asn274, Cys275, Phe276). Of note, Cys275 and Phe276 were consistently broadened in the WT and phosphomimetic variants of NPM1 C70. Altogether, these experiments show that NPM1 C70 phosphomimetic variants kept their ability to interact with Pu24I through the helices α1 and α2, as evidenced by the similar CSP profile (Fig. 3A). Nevertheless, the magnitude of overall CSPs was smaller than for NPM1 C70 WT, suggesting a decrease in DNA binding affinity.

To characterize the thermodynamics of the interactions and assess the binding affinity, ITC measurements were carried out (Fig. 3C and Table 1). The dissociation constant (K_D) value for NPM1 C70 S254D–S260D ($K_D = 9.5 \pm 2.9$ μM) was ca. twice than that of the WT ($K_D = 5.6 \pm 1.7$ μM) species, while it remained similar in NPM1 C70 Y271*p*CMF ($K_D = 4.9 \pm 1.5$ μM; Table 1). This goes in agreement with the smaller CSP values calculated from the NMR titrations. Both phosphomimetic variants display a more favorable enthalpic contribution and a less favorable entropic contribution. In the case of NPM1 C70 S254D–S260D, this might reflect the establishment of stronger polar interactions due to the introduction of negatively charged groups, at the expense of reduced desolvation entropy (as serine is less hydrophilic than aspartate) and a greater loss of conformational entropy upon binding. For NPM1 C70 Y271*p*CMF, this response is likely attributable to the introduction of a negative charge into the phenolic ring.

The addition of negative phosphate charges—mimicked by Asp or *p*CMF substitutions—partially impairs the binding between NPM1 C70 species and DNA. The subtle structural rearrangement of the domain upon phosphomimetic substitution—predicted by MD simulations (Fig. 1C and D) and validated by NMR (Fig. 2)—together with the less-positive DNA-binding interface predicted by ESP calculations (Fig. 1E), may modulate the binding interface through changes in the relative orientation of nearby residue side chains. This is consistent with the shift in the thermodynamic binding profile from entropically to enthalpically driven (Table 1).

NPM1 phosphomimetic variants reshape histone capturing activity and reorganize the homotypic contact network that drives phase separation

The relevance of electrostatically driven intramolecular rearrangements in histone chaperones was recently showcased for *Xenopus laevis* nucleoplasmin (NPM2), another member of the nucleophosmin/nucleoplasmin (NPM) family and close relative of NPM1. The acidic stretches in the flexible tail facilitate recruitment and possibly also entrapment of histone substrates near the acidic surface in the core domain of NPM2

Table 1. Thermodynamic parameters for the interaction of NPM1 C70 WT and its phosphomimetic variants with the Pu24I G-quadruplex oligonucleotide

	K_D (μM)	ΔH (kcal mol^{-1})	–TΔS (kcal mol^{-1})	ΔG (kcal mol^{-1})	n
NPM1 C70 WT	5.6	−2.9	−4.26	−7.2	1.1
NPM1 C70 S254D-S260D	9.5	−6.8	−0.02	−6.8	1.6
NPM1 C70 Y271*p*CMF	4.9	−7.6	−0.39	−7.2	1.1
NPM1 C70 S254D-S260D-Y271*p*CMF	9.5	−1.7	−5.14	−6.8	0.8

K_D, dissociation constant.
ΔG, Gibbs energy of binding.
ΔH and −TΔS, enthalpic and entropic contributions to the Gibbs energy of binding.
Absolute errors: 0.1–0.2 kcal mol^{-1} for ΔG, 0.3–0.5 kcal mol^{-1} for ΔH and −TΔS, and 0.2 for n. Relative error: 20%–30% for K_D.
The stoichiometry (n) for the NPM1 C70-involving complexes is ∼1, except for the S254D–S260D NPM1 C70 variant due to deviations in protein concentration.

[53]. It has been proposed that the C-end basic tract in the IDR of NPM2 shields its largest acidic stretch, hosted in the N-end of the IDR. The competition between the C-end basic tract and histones for the binding to the N-end acidic stretch regulates the histone chaperone activity of NPM2 [54]. Furthermore, phosphorylation of the C-terminal tail of NPM2 enhances nucleosome assembly by promoting histone interaction with the second acidic tract of the protein [55]. In light of the above, we explored whether the phosphorylation of Ser254, Ser260, and Tyr271 in the C-terminal DBD of NPM1 could impact its histone chaperone activity through a similar mechanism.

Therefore, phosphomimetic variants were newly designed in full-length NPM1 (NPM1 FL) and their histone chaperone activity was tested in a histone-capturing disaggregation assay [43, 54]. NPM1 FL species were expressed and purified (Supplementary Fig. S5A), and the incorporation of the noncanonical amino acid *p*CMF in the appropriate position was confirmed by MSMS spectrometry upon trypsin digestion of SDS–PAGE protein bands (Supplementary Fig. S5B). Far-UV CD spectroscopy shows patterns that differ from those of the NPM1 C70 species (Supplementary Fig. S4D). In this case, the pattern was consistent with a protein containing both α-helices and β-sheet motifs, with similar spectra between NPM1 FL WT and phosphomimetic species (Supplementary Fig. S5C).

NPM1 FL species were added at increasing concentrations to a non-nucleosomal histone–DNA aggregate, resulting in the liberation of the DNA contained in them (Fig. 4A–C). The ratio between free and aggregate-contained DNA was computed for each NPM1 FL concentration by quantifying the aggregate-contained DNA band intensity normalized to the intensity of the free DNA control, and data were fit to a linear model (Fig. 4D). In all cases, the ratio of free DNA to aggregated DNA correlated positively (R^2 > 0.9) with increasing amounts of NPM1 FL, indicating that all NPM1 FL phosphomimetic variants retained histone-capturing activity. The S254D–S260D phosphomimetic variant showed the highest disaggregation ability. Counterintuitively, this variant was able to resolve all aggregates at a 0.4 molar ratio (NPM1:H2A/H2B). The underlying mechanism for this behavior remains to be elucidated and may also occur with other variants at different NPM1 FL:H2A/H2B ratios. Ratio 0.4 of NPM1 FL S254D–S260D was omitted for the linear fit. On the contrary, the histone disaggregation ability of the Y271*p*CMF phosphomimetic variant remained similar than that of the WT protein. Control experiments were performed in the absence of H2A/H2B dimers to ensure that the DNA-binding ability of the DBD of NPM1 FL variants did not interfere with the disaggregation assay (Supplementary Fig. S5D).

This finding opens the possibility for the structured C-terminal of the DBD of NPM1 to play an additional role beyond DNA binding, by participating in the (de)shielding of acidic regions within the NPM1 IDR, thereby regulating electrostatic interactions of NPM1 with itself or with its target proteins, such as histones, as a preparatory step for its partitioning into liquid biomolecular condensates [56]. In this context, *in vitro* droplet formation assays were conducted to assess how phosphomimetic substitutions affect the ability of NPM1 FL to undergo phase separation via homotypic interactions, in the presence of Ficoll—a crowding agent that mimics the crowded cellular environment and prompts the formation of NPM1-containing liquid condensates. All NPM1 FL variants were capable of undergoing phase separation. However, the S254D–S260D and Y271*p*CMF variants displayed reduced droplet area occupancy compared to NPM1 WT (Fig. 5A). This suggests that the threshold concentration (C_{sat}) of the variants is expected to be higher than that of the WT. Although the relatively small sample size warrants some caution in interpretation (four replicas used in a Mann–Whitney test), the tendency was consistent across the entire tested protein concentration range for the NPM1 FL Y271*p*CMF, whereas statistically significant differences for the S254D–S260D variant were limited to the 0.25–2.5 μM protein concentration range.

At higher protein concentrations, NPM1 FL Y271*p*CMF exhibited reduced wetting on hydrophobic glass surfaces (Fig. 5B), indicating that the Tyr271-to-*p*CMF substitution further altered the physicochemical properties of the resulting biomolecular condensates. These results suggest that phosphorylation of the structured C-terminal DBD of NPM1 partially neutralizes the adjacent block of positive charges in the unstructured central region of the protein, as revealed by ESP maps (Fig. 1E). This modulation reduces "charge blockiness" throughout NPM1 IDR, thereby decreasing its propensity for LLPS [57].

Concomitant Ser254, Ser260, and Tyr271 phosphomimetic substitutions in the NPM1 DNA binding domain prompts its aggregation, limits both nucleic acids binding and charge block-driven phase transition

To delve deeper into the effect of a triple phosphorylation at Ser254, Ser260, and Tyr271, we ran MD simulations of an NPM1 C70 S254D–S260D–Y271*p*CMF triple variant. The results were in good agreement with the other phosphomimetic species analyzed, where three α-helical tracts were observed, which were still less stable when compared to NPM1 C70 WT (Supplementary Fig. S2D).

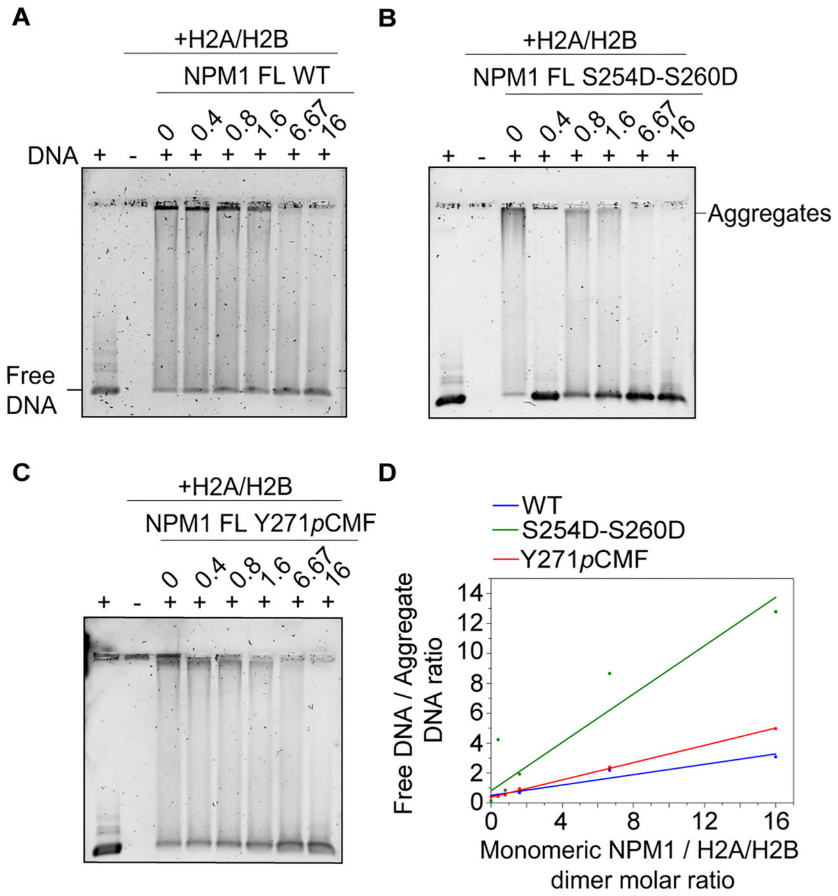

Figure 4. Histone-capture activity of FL NPM1 phosphomimetic variants. Histone-capture disaggregation assays for NPM1 FL WT (**A**), NPM1 FL S254D–S260D (**B**), and NPM1 FL Y271*p*CMF (**C**). NPM1 FL to H2A/H2B ratios are indicated above each gel lane. (**D**) Free-to-aggregate DNA ratio values as a function of NPM1 FL concentration. Data were fit to a linear model. The ratio value of 0.4 for NPM1 FL S254D–S250D was excluded from the fitting. Adjusted R^2 values for the fittings were 0.934 (WT), 0.917 (S254D–S260D), and 0.998 (Y271*p*CMF).

The mean distances between all residue pairs in the three-helix bundle along the MD simulation time were compared between NPM1 C70 S254D–S260D–Y271*p*CMF and the WT species to identify the residues approaching or diverging upon substitution (Fig. 6A). After selecting the residue pairs with the highest mean distance difference ($>\mu + 3\sigma$), 15 pairs stood out, where residues belonging to the domain's hydrophobic core were notably involved. The hydrophobic core of NPM1 C-end domain is mainly formed by four aromatic residues (Phe268, Phe276, Trp288, and Trp290) [58]. However, residues such as Ile247, Tyr271, Val272, or Leu287 also contribute to the formation of the hydrophobic pocket, whose compact nature is crucial for the architecture of the domain [59]. Following the residue distance analysis, Trp288 and Trp290 were included in seven of the identified pairs, more abundantly than in the other phosphomimetic variants. Interestingly, the distance between both Trp residues and Asp260, as well as between Trp290 and *p*CMF271, increased significantly. Of the remaining residue pairs, four of them included *p*CMF271, whose distance from residues belonging to helix α1 (Lys248, Ala249, Met251, and Gln252) also increased. Altogether, MD simulations data suggest that the interference of phosphomimetic sites (Asp260 and *p*CMF271) with α1 and the NoLS Trp residues loosens the contacts in the hydrophobic core of the domain. The behavior of the triple-phosphorylated NPM1 C70 domain in MD simulations aligned with findings observed for the triple phosphomimetic variant (Supplementary Fig. S3C and D).

The S254D–S260D–Y271*p*CMF triple variant in both NPM1 C70 and NPM1 FL constructs was then expressed, purified, and characterized (Supplementary Figs S4A and S5A). Far-UV CD spectra of NPM1 C70/FL WT and NPM1 C70/FL triple variant were similar, indicating a comparable secondary structure content between the WT and phosphomimetic species (Supplementary Figs S4D and S5C). However, most of the protein backbone amide resonance in the [^{1}H, ^{15}N]-HSQC NMR spectrum of the NPM1 C70 triple variant collapsed at 8.0 ppm at temperatures higher than 298 K (Fig. 6B, upper). Intriguingly, when the temperature is decreased down to 278 K a gradual detection of amide resonance signals occurs, matching the ones registered for other NPM1 C70 phosphomimetic species (Fig. 6B, lower). Comparing the signals of three backbone amide resonances and the ϵ-amide group of Trp288 in the ^{15}N-HSQC spectra of NPM1 C70 WT and triple variant (Supplementary Fig. S6A–C), there was an increase in the range of 5.5–15.0 Hz in ^{1}H frequency linewidth of such resonances from the triple variant with respect to the ones from the WT construct. This is consistent with the aggregation propensity of NPM1 C70 S254D–S260D–Y271*p*CMF.

CD-monitored thermal denaturation profiles of both NPM1 C70 WT and triple variant were consistent with a single thermal transition between folded and denatured states

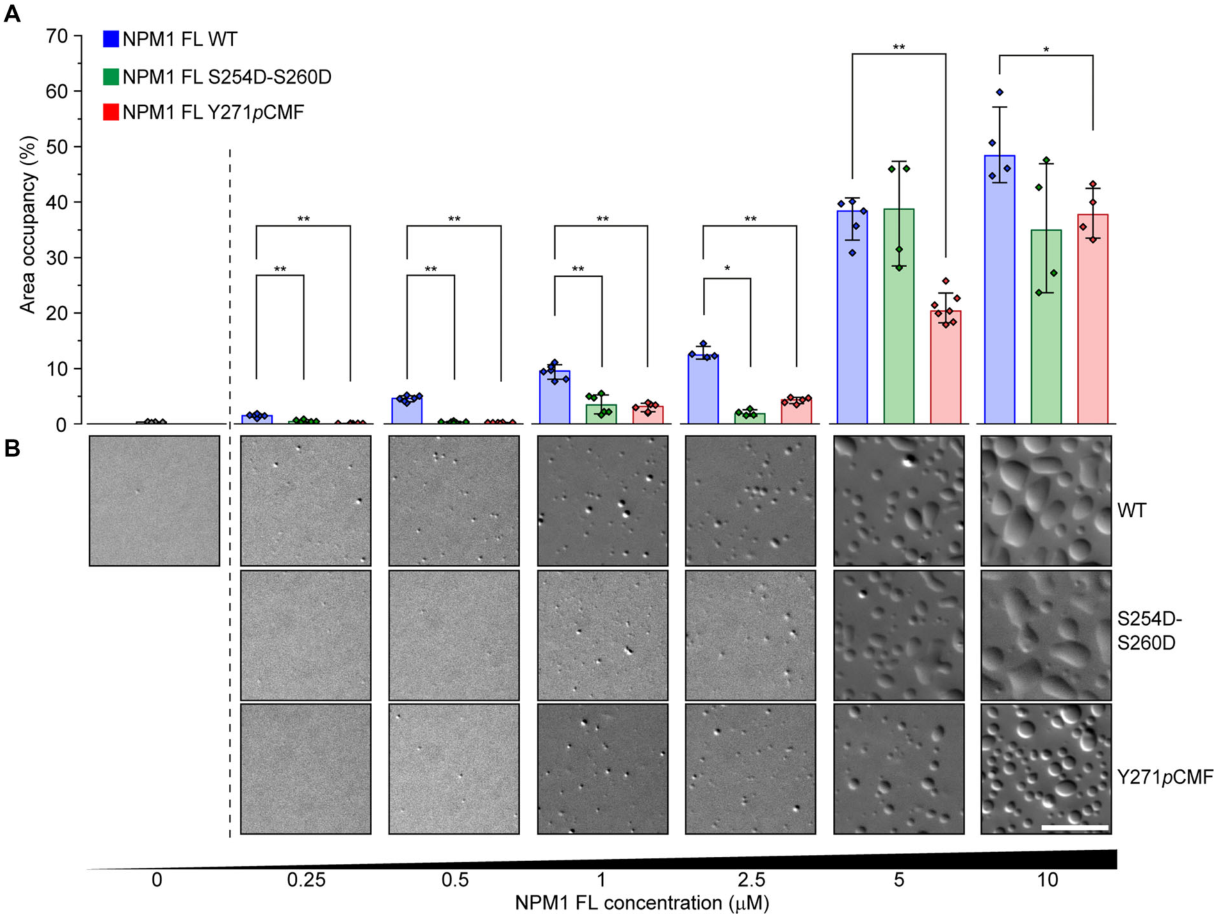

Figure 5. Homotypic LLPS of NPM1 FL phosphomimetic variants. (**A**) Percentage of area in the microscopy fields occupied by protein condensates of NPM1 FL WT, NPM1 FL S254D–S260D and NPM1 FL Y271*p*CMF phosphomimetic variants as a function of protein concentration (pentamer). The top of the bars represents the median values of the distributions and error bars show ± one standard deviation. Statistically significant differences are indicated: P-value <.05 (∗), P-value <.01 (∗∗). (**B**) Microscopy images of biomolecular condensates of NPM1 FL WT, NPM1 FL S254D–S260D, and NPM1 FL Y271*p*CMF phosphomimetic variants as a function of protein concentration. For display purposes images are zoomed in to show roughly 5% of the total surface of the microscopy field and intensity levels were autoscaled for each image. Scale bars: 20 μm.

(Fig. 6C). However, NPM1 C70 S254D–S26D–Y271*p*CMF exhibited a much lower thermal stability, with a melting temperature (T_m) ca. 15°C lower than that of NPM1 C70 WT. At 37°C, the triple variant exhibited a 26% reduction in the fraction of folded protein compared with the WT, decreasing from 94% to 68%.

The differential stability of the two proteins was further confirmed by REST2 simulations, which revealed distinct stability profiles for the NPM1 C70 wild type and its mutant variant (Supplementary Fig. S7). The mutant exhibited a steeper decline in the fraction of folded states compared to the wild type, indicating reduced thermal stability. Notably, the calculated melting temperature (T_m) difference between the wild type and mutant equal to 41 K, in line with the experimental data, falling within the expected deviation of the computational approach [37, 60].

Altogether, these data suggest that NPM1 C70 triple variant is folded, in agreement with the far-UV CD spectrum, but it is prone to aggregate at physiological temperature, as inferred from the loss of dispersion and the increase in linewidths of the NMR backbone amide resonances.

ESP alterations were more pronounced than those observed in other variants, rendering the entire DNA-binding surface of the domain, as well as the neighboring unstructured N-terminal stretch, noticeably less positively charged (Fig. 6D). This effect was further amplified in the triple-phosphorylated variant (Supplementary Fig. S3E). Further ITC experiments with NPM1 C70 S254D–S260D–Y271*p*CMF and Pu24I oligo yielded approximately a two-fold decrease in DNA binding affinity ($K_D = 9.5 \pm 2.9$ μM) compared to NPM1 C70 WT, albeit the binding was entropically driven in both NPM1 C70 species (Fig. 6E and Table 1). A less favorable enthalpic contribution and a more favorable entropic contribution may reflect weaker polar interactions resulting from the accumulation of negatively charged groups, leading to a suboptimal binding interface that retains some polar group mobility and undergoes a smaller loss of conformational entropy upon binding. This provides a clear example of the nonadditive effects of modifications and the context-dependent impact of structural changes on protein binding affinity. Histone-capturing activity was also the lowest out of all NPM1 FL species studied, although similar to that of NPM1 FL WT (Fig. 6F and Supplementary Fig. S6D).

Disruption of charge segregation along the IDR in the NPM1 triple phosphomimetic variant partially impairs charge block-driven LLPS [57]. Consistently, NPM1 FL S254D–S260D–Y271*p*CMF exhibited significantly reduced droplet area occupancy compared to NPM1 FL WT across the

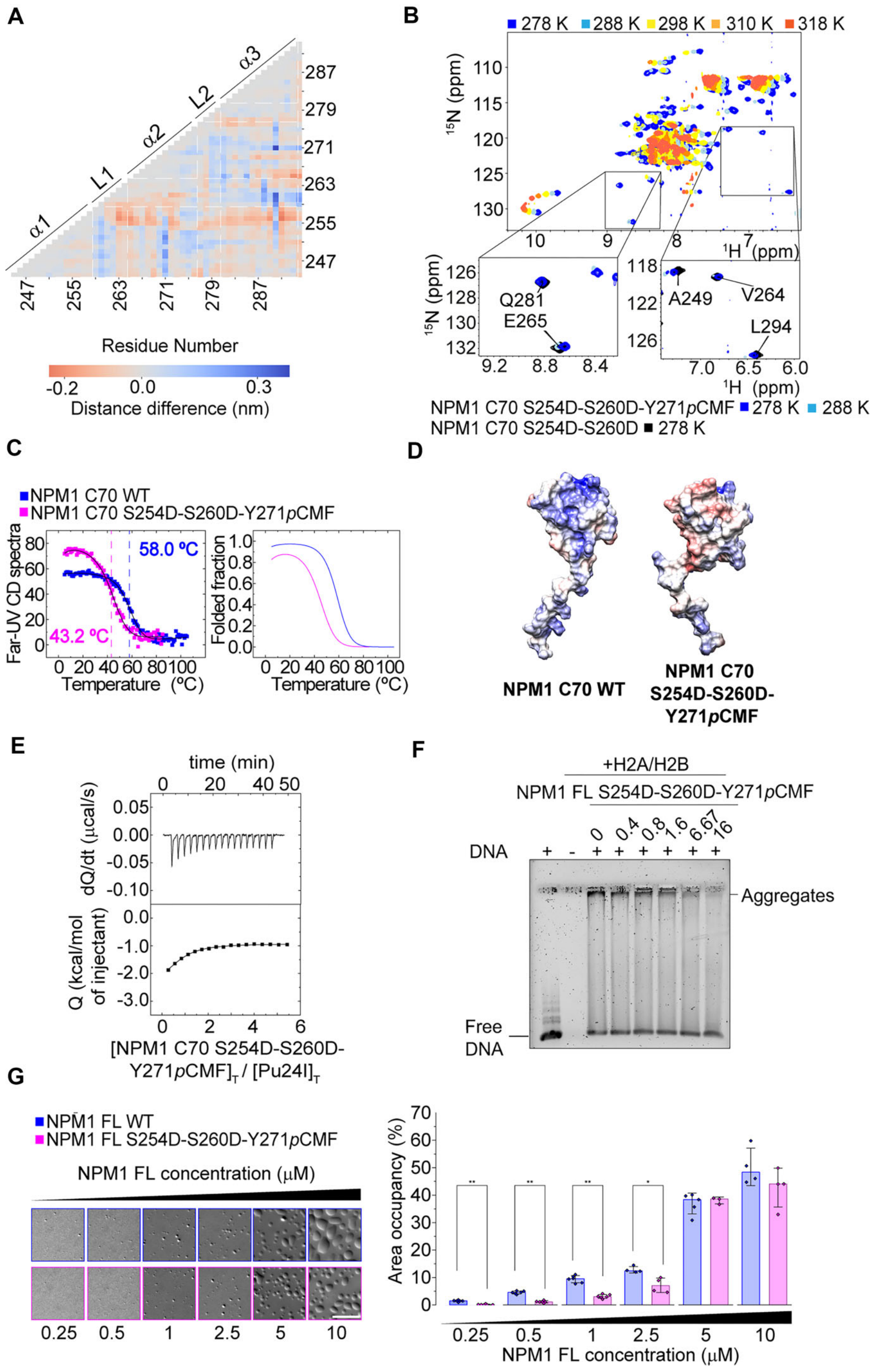

Figure 6. *In silico* molecular dynamics calculations, biophysical characterization, DNA binding, histone-capture disaggregation, and liquid droplets assays of the NPM1 C70/FL S254D–S260D–Y271*p*CMF triple variant. (**A**) Heatmap showing the mean distance differences between all residue pairs in the three-helix bundle of NPM1 C70 WT and the triple variant. Mean distances were calculated from sampled frames of two different replicates for each variant. Residue pairs that distance from each other are in blue, whereas those that come closer are in red. (**B**) Overlayed ^{15}N-HSQC spectra of NPM1 C70 S254D–S260D–Y271*p*CMF at different temperatures (upper) with insets highlighting signals visible only at lower temperatures, corresponding to similar ones observed in the NPM1 C70 S254D–S260D spectra (lower). (**C**) Left, CD-monitored thermal denaturation profile of NPM1 C70 WT and the S254D–S260D–Y271*p*CMF triple variant derived from the projection of the first principal component. Nonlinear regression data analysis applying the single transition model was used. Dashed lines indicate the T_m values for WT (58.0°C) and the triple variant (43.2°C). Right, fraction of folded protein as a function of temperature during CD-monitored thermal denaturation. (**D**) ESP comparison between NPM1 C70 WT and the S254D–S260D–Y271*p*CMF triple variant, based on MD simulation frames. The scale ranges from −5 (red) to +5 (blue) K_B *T/e*. (**E**) ITC assay with the NPM1 C70 S254D–S260D–Y271*p*CMF triple variant and the G-quadruplex c-myc promoter Pu24I. The thermogram (upper) and the calculated binding isotherm (lower) are shown. (**F**) Histone-capture disaggregation assay for the NPM1 C70 S254D–S260D–Y271*p*CMF triple variant. (**G**) Left, microscopy images of biomolecular condensates of NPM1 FL WT and S254D–S260D–Y271*p*CMF phosphomimetic variant as a function of protein concentration. For display purposes, images are zoomed in to show roughly 5% of the total surface of the microscopy field and intensity levels were autoscaled for each image. Scale bars: 20 μm. Right, percentage of area in the microscopy fields occupied by protein condensates of NPM1 FL WT and S254D–S260D–Y271*p*CMF phosphomimetic variant as a function of protein concentration (pentamer). The top of the bars represents the median values of the distributions and error bars show ± one standard deviation. Statistically significant differences are indicated: *P*-value <.05 (∗), *P*-value <.01 (∗∗).

0.25–2.5 μM concentration range (Fig. 6G), accompanied by a slight decrease in droplet wetting. These results suggest a multifunctional role for the phosphorylations on NPM1 C-end domain, which modulate not only its ability to integrate into the nucleolus via homo- and heterotypic LLPS but also its histone chaperone activity when populating the nucleoplasm.

Discussion

Phosphorylation events play a critical role in regulating NPM1 function [21]. While phosphorylation sites are distributed along the entire length of the protein, the AML-related C-terminal DBD serves as a key hub for these modifications [20, 22]. Phosphorylation at specific residues of the domain has been associated with the translocation of NPM1 from the nucleolus to the nucleoplasm [20, 22]. NPM1 integrates into the nucleolus by establishing an intricate network of self-interactions (homotypic) and interactions with other proteins and nucleic acids (heterotypic), thereby providing the multivalency required for LLPS and driving the organization of the membrane-less organelle into coexisting, immiscible liquid phases [56]. Both homotypic and heterotypic LLPS mechanisms in NPM1 are predominantly electrostatically driven. Homotypic interactions rely on the interplay between acidic and basic tracts within NPM1, whereas heterotypic interactions involve the binding of NPM1 acidic regions to positively charged protein motifs or, alternatively, the association of its basic tracts and DBD with nucleic acids [56]. The structural integrity of the DBD is also essential for nucleic acid recognition, a property that is lost upon unfolding induced by type A AML mutations [61]. Thus, the dynamic interplay among protein stability, DNA binding, and charge block-mediated phase separation ultimately determines NPM1 localization and functional output.

Given that the behavior of NPM1 is dependent on its charge block distribution, the negative charges introduced by phosphorylation in the basic DBD are likely to disrupt its interaction with nucleic acids and acidic tracts within the protein, ultimately driving NPM1 displacement from the nucleolus. In this work, we investigated the effects of phosphorylation at Ser254, Ser260, and Tyr271 on the NPM1 DBD, using the NPM1 C70—Pu24I as a model system.

MD simulations provided insight into the dynamic behavior of the NPM1 C-terminal three-helix bundle. Phosphomimetic amino acid substitutions at specific positions within this motif induced a destabilizing effect that propagated across all three helices. Although mild destabilization of the C-terminal region was occasionally observed, the three NPM1 C70 variants—S254D–S260D, Y271*p*CMF and S254D–S260D–Y271*p*CMF—retained the global folding of the domain, as later confirmed by CD and NMR experiments. The slight fluctuations in secondary structure observed during MD simulations likely reflects the bundle's attempts to accommodate the introduction of negative charges near its hydrophobic core. Simulations were extended to 2 μs to explore the conformational space more thoroughly. Overall, our MD simulations data suggest that, despite its compact arrangement, the NPM1 C-terminal three-helix bundle is sufficiently dynamic to rearrange and allow for phosphorylation to occur at the studied positions. In line with this, our CD and NMR experiments confirmed that the phosphomimetic variants remained folded into an α-helix-containing structure. However, the chemical environment of residues at helices α1 and α2 still undergoes significant perturbations in both NPM1 C70 S254D–S260D and Y271*p*CMF variants. This is consistent with the observation that phosphomimetic substitutions primarily affect the interface between these two α-helices. The maintenance of contacts between the helices is crucial for G-quadruplex binding. The loss of compactness associated with the AML-type A-mutated NPM1 C-terminal domain partly explains its inability to bind DNA [61].

Interestingly, when S254D, S260D, and Y271*p*CMF mutations are combined in the NPM1 C70 construct, the resulting protein exhibits an increased aggregation propensity. This is likely due to an alteration of the NPM1 C70 hydrophobic core, involving Trp288 and Trp290. The fact that aggregation only occurs when all three substitutions are present suggests a model in which domain destabilization is driven by cooperative, multisite phosphorylation, similar to the model proposed for the NPM1 N-terminal oligomerization domain [62]. In that case, sequential phosphorylations modulate the equilibrium between the ordered pentamer and disordered monomers [62]. The domain instability within the context of the FL NPM1 protein and its reversibility remains to be explored.

Moreover, the Ser-to-Asp and Tyr-to-*p*CMF substitutions directly affect Pu24I DNA binding site. The DNA-binding groove is similar among NPM1 C70 variants, but it is less-positively charged in the phosphomimetic variants compared to the WT counterpart. This affects DNA recognition, as complex formation is primarily electrostatically driven through interactions between key residues of the three-helix bundle and the phosphate groups of Pu24I [24], with the aid of the adjacent unstructured stretch [63]. According to our biophysical characterization of the nucleic acid–protein interaction, the NPM1 C70 phosphomimetic variants are still able to bind G-quadruplex structures, although with decreased affinity in the case of the S254D–S260D variant. Nucleic acid binding is known to be critical for the nucleolar localization of NPM1, as loss of binding to rDNA G-quadruplex structures has been shown to displace the protein from the nucleolus [61]. Interestingly, the K_D values reported for the wild-type NPM1 C70 domain binding to multiple G-quadruplex rDNA sequences [61] align well with the observed values for binding of NPM1 phosphomimetic variants to the G-quadruplex Pu24I DNA. In a multicellular context, Chiarella *et al.* [61] also demonstrated that treatment with TmPyP4, a well-known G-quadruplex ligand, displaces endogenous NPM1 to the nucleoplasm in the OCI-AML2 cell line, mirroring the localization observed for the S254D–S260D and Y271-phosphorylated NPM1 variants under cellular stress [20, 22]. Together, these findings suggest that, although the binding affinity is relatively modest, it is nonetheless biologically relevant in determining NPM1 cellular localization. Additionally, disruption of G-quadruplex structures in the lncRNA MALAT1 compromises NPM1 localization to nuclear speckles [50]. Furthermore, interaction of NPM1 with nucleolar nucleic acids (i.e. rRNA) is essential for LLPS mechanisms mediated by heterotypic contacts that facilitate protein integration into the organelle [64].

Although the oligomerization and DNA binding domains of NPM1 are separated by the long IDR, they should not be considered as independently acting entities. Intramolecular interactions between basic and acidic stretches that affect protein function have already been described in other members of the nucleophosmin/nucleoplasmin family [54, 55]. Here, we show that phosphomimetic variants in the C-terminal domain of FL NPM1 display significant differences in their histone-capturing activity. While NPM1 FL Y271*p*CMF has similar activity to that of the WT protein, the S254D–S260D phosphomimetic variant is much more effective in resolving the DNA-histones aggregates. We hypothesize that the addition of two negative charges in the basic C-terminal DBD is necessary to prevent the intramolecular shielding between the histone-binding acidic and C-terminal basic stretches in the IDR of NPM1, in a manner similar to what has been described for *Xenopus laevis* NPM2 [54]. We also propose that the structured C-end DBD contributes to the electrostatically driven homotypic phase separation of NPM1 [56], acting within the interplay of acidic and basic charge blocks along the protein. As suggested from ESP maps, phosphorylation of Ser and/or Tyr within the DBD may influence the N-end adjacent basic stretch, thereby partially disrupting the characteristic charge segregation pattern of the NPM1 IDR that underlies its ability to undergo LLPS [57]. NPM1 oligomerization is also a key determinant in regulating droplet formation [65], whose fluidity depends on the stability of the pentamer. Crosstalk between NPM1's oligomerization and DBDs and its acidic histone-binding stretch underlies the protein's phase partitioning behavior, with the structured domains emerging as cornerstones in LLPS.

When the combined effect of all three phosphomimetic substitutions converges in the S254D–S260D–Y271*p*CMF variant, its histone-capturing activity is slightly reduced compared to that of NPM1 FL WT. Similarly, the homotypic LLPS exhibited by the triple variant mirrors that of the S254D–S260D variant. Together, these findings point to a dual role for C-end DBD phosphorylation: fine-tuning transient contacts with acidic regions involved in histone chaperoning, and dampening "charge blockiness" within the IDR, thereby modulating NPM1's ability to undergo homotypic phase separation—where Ser254 and Ser260 act as drivers, and Tyr271 functions as a repressor. Altogether, these findings suggest that the three phosphorylation sites are important contributors to NPM1 redistribution, though not the sole ones. Such phosphorylation events may act in concert with additional modifications—for instance, Tyr271 phosphorylation has been detected together with phosphorylation at Tyr17, Tyr29, and Tyr67 [20]. We therefore propose that NPM1 localization within the cell is regulated by the synergistic interplay of cumulative modifications across distinct regions of the protein.

Altogether, we show that the NPM1 C-terminal DBD displays intrinsic dynamics that allow the three-helix bundle to adapt to independent phosphorylation events at Ser254, Ser260, or Tyr271. However, this domain experiences a remarkable destabilization when these modifications occur simultaneously. Preservation of a folded structure upon addition of negative charges in the $\alpha1$ and $\alpha2$ interface allows the phosphomimetic variants to still bind G-quadruplex structures. Nonetheless, both structural constraints and marked alterations in ESP maps account for the reduced DNA affinity of NPM1 variants, as well as the diminished segregation of acidic and basic charge blocks within the IDR. Given that both homo- and heterotypic interactions are key to NPM1's phase separation and nucleolar retention, the combined effects of reduced DNA-binding affinity, altered binding mechanisms, diminished droplet-forming capacity, and increased domain instability offer a compelling molecular explanation for how simultaneous phosphorylation at Ser254, Ser260, and Tyr271 could drive NPM1 displacement from the nucleolus.

Acknowledgements

The authors would like to thank the staff at the NMR facility at the Research, Technology and Innovation center of the University of Seville (CITIUS), the BIO-MS laboratory (UPO), and the microscopy, chromatography, imaging, and centrifuges services at the Institute of Plant Biochemistry and Photosynthesis (IBVF), and the Biomolecular Interaction Platform (cicCartuja, Seville). We are also grateful to the GENCI France supercomputers for generous allocation of GPU time.

Author Contributions: Pablo Rivero-García (Conceptualization [equal], Data curation [equal], Formal analysis [equal], Investigation [equal], Methodology [equal], Writing – original draft [equal]), Rafael Luis Giner-Arroyo (Conceptualization [equal], Investigation [equal], Methodology [equal], Writing – original draft [equal]), Joaquín Tamargo-Azpilicueta (Conceptualization [equal], Investigation [equal], Methodology [equal], Writing – original draft [equal]), Abbey Telfer (Data curation [equal], Formal analysis [equal], Writing – original draft [equal]), Elisa Frezza (Formal analysis [equal], Investigation [equal]), Adrián Velázquez-Campoy (Formal analysis [equal], Investigation [equal], Writing – original draft [equal]), Sofía Díaz-Moreno (Conceptualization [equal], Investigation [equal], Supervision [equal], Writing – review & editing [equal]), Miguel Angel De la Rosa (Conceptualization [equal], Funding acquisition [equal], Investigation [equal], Project administration [equal], Supervision [equal], Writing – review & editing [equal]), and Irene Díaz-Moreno (Conceptualization [equal], Funding acquisition [equal], Investigation [equal], Methodology [equal], Project administration [equal], Resources [equal], Supervision [equal], Writing – original draft [equal], Writing – review & editing [equal])

Supplementary data

Supplementary data is available at NAR online.

Conflict of interest

None declared.

Funding

This work was supported by the Spanish State Research Agency (AEI), Spanish Ministry of Science, Innovation and Universities (MCIU) and "ERDF A way of making Europe" (MCIU/AEI/10.13039/501100011033, grant numbers PID2024-157414NB-I00, PRE2019-091404 to R.G.-A., FPU22/01094 to J.T.-A., and FPU24/00691 to P.R.-G.); Ramon Areces Foundation (LEUCYTO-FRA2025-MAR); Spanish Ministry of Education, Vocational Training and Sports (23CO1/008490 to P.R.-G.); and Spanish Council of Scientific Research (JAEINT24_EX_0171 to P.R.-G.). Funding for open access charge: Universidad de Sevilla (Biblioteca Universidad de Sevilla) has an agreement with Oxford University Press, including the 100% cover of Open Access publication in Nucleic Acids Research.

Data availability

The data underlying this article are available in the article and in its online supplementary material or will be shared on reasonable request to the corresponding author. The assignment data are available in BMRB and can be accessed with 52438 and 52439 deposition numbers. Mass spectrometry data are publicly available via Zenodo, https://doi.org/10.5281/zenodo.18598163.

References

1. De Kouchkovsky I, Abdul-Hay M. Acute myeloid leukemia: a comprehensive review and 2016 update. *Blood Cancer J* 2016;6:e441. https://doi.org/10.1038/bcj.2016.50
2. Döhner H, Wei AH, Appelbaum FR *et al.* Diagnosis and management of AML in adults: 2022 recommendations from an international expert panel on behalf of the ELN. *Blood* 2022;140:1345–77.
3. Khoury JD, Solary E, Abla O *et al.* The 5th edition of the World Health Organization classification of haematolymphoid tumours: myeloid and histiocytic/dendritic neoplasms. *Leukemia* 2022;36:1703–19. https://doi.org/10.1038/s41375-022-01613-1
4. Sharma N, Liesveld JL. NPM 1 mutations in AML—the landscape in 2023. *Cancers* 2023;15:1177. https://doi.org/10.3390/cancers15041177
5. Buzón P, Velázquez-Cruz A, Corrales-Guerrero L *et al.* The histone chaperones SET/TAF-1β and NPM1 exhibit conserved functionality in nucleosome remodeling and histone eviction in a cytochrome c-dependent nanner. *Adv. Sci.* 2023;10:2301859.
6. Box JK, Paquet N, Adams MN *et al.* Nucleophosmin: from structure and function to disease development. *BMC Mol Biol* 2016;17:19. https://doi.org/10.1186/s12867-016-0073-9
7. Papaemmanuil E, Gerstung M, Bullinger L *et al.* Genomic classification and prognosis in acute myeloid leukemia. *N Engl J Med* 2016;374:2209–21. https://doi.org/10.1056/NEJMoa1516192
8. Ley TJ, Miller C, Ding L *et al.* Genomic and epigenomic landscapes of adult *de novo* acute myeloid leukemia. *N. Engl. J. Med.* 2013;368:2059–74.
9. Patel JP, Gönen M, Figueroa ME *et al.* Prognostic relevance of integrated genetic profiling in acute myeloid leukemia. *N Engl J Med* 2012;366:1079–89. https://doi.org/10.1056/NEJMoa1112304
10. Falini B, Martelli MP, Bolli N *et al.* Acute myeloid leukemia with mutated nucleophosmin (NPM1): is it a distinct entity? *Blood* 2011;117:1109–20. https://doi.org/10.1182/blood-2010-08-299990
11. Falini B, Alcalay M, Starza RL *et al.* Cytoplasmic nucleophosmin in acute myelogenous leukemia with a normal karyotype. *N Engl J Med* 2005;352:254–66. https://doi.org/10.1056/NEJMoa041974
12. Grummitt CG, Townsley FM, Johnson CM *et al.* Structural consequences of nucleophosmin mutations in acute myeloid leukemia. *J Biol Chem* 2008;283:23326–32. https://doi.org/10.1074/jbc.M801706200
13. Hingorani K, Szebeni A, Olson MOJ. Mapping the functional domains of nucleolar protein B23. *J Biol Chem* 2000;275:24451–7. https://doi.org/10.1074/jbc.M003278200
14. Federici L, Arcovito A, Scaglione GL *et al.* Nucleophosmin C-terminal leukemia-associated domain interacts with G-rich quadruplex forming DNA. *J Biol Chem* 2010;285:37138–49. https://doi.org/10.1074/jbc.M110.166736
15. Falini B, Bolli N, Shan J *et al.* Both carboxy-terminus NES motif and mutated tryptophan(s) are crucial for aberrant nuclear export of nucleophosmin leukemic mutants in NPMc$^+$ AML. *Blood* 2006;107:4514–23. https://doi.org/10.1182/blood-2005-11-4745
16. Nishimura Y, Ohkubo T, Furuichi Y *et al.* Tryptophans 286 and 288 in the C-terminal region of protein B23.1 are important for its nucleolar localization. *Biosci Biotechnol Biochem* 2002;66:2239–42. https://doi.org/10.1271/bbb.66.2239
17. Bolli N, Nicoletti I, De Marco MF *et al.* Born to be exported: cOOH-terminal nuclear export signals of different strength ensure cytoplasmic accumulation of nucleophosmin leukemic mutants. *Cancer Res* 2007;67:6230–7. https://doi.org/10.1158/0008-5472.CAN-07-0273
18. Falini B, Brunetti L, Sportoletti P *et al.* NPM1-mutated acute myeloid leukemia: from bench to bedside. *Blood* 2020;136:1707–21. https://doi.org/10.1182/blood.2019004226
19. Ianni A, Kumari P, Tarighi S *et al.* SIRT7-dependent deacetylation of NPM promotes p53 stabilization following UV-induced genotoxic stress. *Proc Natl Acad Sci USA* 2021;118:e2015339118. https://doi.org/10.1073/pnas.2015339118
20. Russo LC, Ferruzo PYM, Forti FL. Nucleophosmin protein dephosphorylation by DUSP3 is a fine-tuning regulator of p53 signaling to maintain genomic stability. *Front Cell Dev Biol.* 2021;9:624933. https://doi.org/10.3389/fcell.2021.624933
21. Karimi Dermani F, Gholamzadeh Khoei S, Afshar S *et al.* The potential role of nucleophosmin (NPM1) in the development of cancer. *J Cell Physiol* 2021;236:7832–52. https://doi.org/10.1002/jcp.30406
22. Sridharan S, Hernandez-Armendariz A, Kurzawa N *et al.* Systematic discovery of biomolecular condensate-specific protein phosphorylation. *Nat Chem Biol* 2022;18:1104–14. https://doi.org/10.1038/s41589-022-01062-y
23. González-Arzola K, Díaz-Quintana A, Bernardo-García N *et al.* Nucleus-translocated mitochondrial cytochrome c liberates nucleophosmin-sequestered ARF tumor suppressor by changing nucleolar liquid–liquid phase separation. *Nat Struct Mol Biol* 2022;29:1024–36. https://doi.org/10.1038/s41594-022-00842-3
24. Gallo A, Lo Sterzo C, Mori M *et al.* Structure of nucleophosmin DNA-binding domain and analysis of its complex with a G-quadruplex sequence from the c-MYC promoter. *J Biol Chem* 2012;287:26539–48. https://doi.org/10.1074/jbc.M112.371013
25. Guerra-Castellano A, Díaz-Quintana A, Moreno-Beltrán B *et al.* Mimicking tyrosine phosphorylation in human cytochrome c by the evolved tRNA synthetase technique. *Chemistry* 2015;21:15004–12. https://doi.org/10.1002/chem.201502019
26. Luger K, Rechsteiner TJ, Richmond TJ. Preparation of nucleosome core particle from recombinant histones. *Methods Enzymol* 1999;304:3–19.
27. Tian C, Kasavajhala K, Belfon AA *et al.* ff19SB: amino-acid-specific protein backbone parameters trained against quantum mechanics energy surfaces in solution. *J. Chem. Theory Comput.* 2020;16:528–52. https://doi.org/10.1021/acs.jctc.9b00591
28. Homeyer N, Horn AHC, Lanig H *et al.* AMBER force-field parameters for phosphorylated amino acids in different protonation states: phosphoserine, phosphothreonine, phosphotyrosine, and phosphohistidine. *J Mol Model* 2006;12:281–9. https://doi.org/10.1007/s00894-005-0028-4
29. Eastman P, Swails J, Chodera JD *et al.* OpenMM 7: rapid development of high performance algorithms for molecular dynamics. *PLoS Comput Biol* 2017;13:e1005659. https://doi.org/10.1371/journal.pcbi.1005659
30. Roe DR, Cheatham TE. PTRAJ and CPPTRAJ: software for processing and analysis of molecular dynamics trajectory data. *J Chem Theory Comput* 2013;9:3084–95. https://doi.org/10.1021/ct400341p
31. McGibbon RT, Beauchamp KA, Harrigan MP *et al.* MDTraj: a modern open library for the analysis of molecular dynamics trajectories. *Biophys J* 2015;109:1528–32. https://doi.org/10.1016/j.bpj.2015.08.015
32. Wang L, Friesner RA, Berne BJ. Replica exchange with solute scaling: a more efficient version of replica exchange with solute tempering (REST2). *J. Phys. Chem. B* 2011;115:9431–8. https://doi.org/10.1021/jp204407d
33. Abraham MJ, Murtola T, Schulz R *et al.* GROMACS: high performance molecular simulations through multi-level parallelism from laptops to supercomputers. *SoftwareX* 2015;1-2:19–25. https://doi.org/10.1016/j.softx.2015.06.001
34. Tribello GA, Bonomi M, Branduardi D *et al.* PLUMED 2: new feathers for an old bird. *Comput Phys Commun* 2014;185:604–13. https://doi.org/10.1016/j.cpc.2013.09.018

35. Shirts MR, Klein C, Swails JM *et al.* Lessons learned from comparing molecular dynamics engines on the SAMPL5 dataset. *J Comput Aided Mol Des* 2017;31:147–61. https://doi.org/10.1007/s10822-016-9977-1
36. Bussi G. Hamiltonian replica exchange in GROMACS: a flexible implementation. *Mol Phys* 2014;112:379–84. https://doi.org/10.1080/00268976.2013.824126
37. Stirnemann G, Sterpone F. Recovering protein thermal stability using all-atom hamiltonian replica-exchange simulations in explicit solvent. *J Chem Theory Comput* 2015;11:5573–7. https://doi.org/10.1021/acs.jctc.5b00954
38. Jakalian A, Jack DB, Bayly CI. Fast, efficient generation of high-quality atomic charges. AM1-BCC model: II. Parameterization and validation. *J Comput Chem* 2002;23:1623–41. https://doi.org/10.1002/jcc.10128
39. Pettersen EF, Goddard TD, Huang CC *et al.* UCSF Chimera—a visualization system for exploratory research and analysis. *J Comput Chem* 2004;25:1605–12. https://doi.org/10.1002/jcc.20084
40. Jurrus E, Engel D, Star K *et al.* Improvements to the APBS biomolecular solvation software suite. *Protein Sci* 2018;27:112–28. https://doi.org/10.1002/pro.3280
41. Humphrey W, Dalke A, Schulten K. VMD: visual molecular dynamics. *J Mol Graphics* 1996;14:33–8. https://doi.org/10.1016/0263-7855(96)00018-5
42. Manthey I, Tonelli M, Ii LC *et al.* POKY software tools encapsulating assignment strategies for solution and solid-state protein NMR data. *J Struct Biol X* 2022;6:100073.
43. Lorton BM, Warren C, Ilyas H *et al.* Glutamylation of Npm2 and Nap1 acidic disordered regions increases DNA charge mimicry to enhance chaperone efficiency. *iScience* 2024;27:109458. https://doi.org/10.1016/j.isci.2024.109458
44. Schneider CA, Rasband WS, Eliceiri KW. NIH Image to ImageJ: 25 years of image analysis. *Nat Methods* 2012;9:671–5. https://doi.org/10.1038/nmeth.2089
45. Casado-Combreras MÁ, Velázquez-Campoy A, Martinho M *et al.* Cytochrome c prompts the recruitment of its nuclear partners SET/TAF-Iβ and NPM1 into biomolecular condensates. *iScience* 2024;27:110435. https://doi.org/10.1016/j.isci.2024.110435
46. Casado-Combreras MÁ, De La Rosa MA, Díaz-Moreno I. Protocols for monitoring condensate formation and dynamics between the phase-separating proteins SET/TAF-Iβ and cytochrome c. *STAR Protoc* 2025;6:103796. https://doi.org/10.1016/j.xpro.2025.103796
47. Chen Z, Cole PA. Synthetic approaches to protein phosphorylation. *Curr Opin Chem Biol* 2015;28:115–22. https://doi.org/10.1016/j.cbpa.2015.07.001
48. Pérez-Mejías G, Velázquez-Cruz A, Guerra-Castellano A *et al.* Exploring protein phosphorylation by combining computational approaches and biochemical methods. *Comput Struct Biotechnol J* 2020;18:1852–63.
49. Wang D, Baumann A, Szebeni A *et al.* The nucleic acid binding activity of nucleolar protein B23.1 resides in its carboxyl-terminal end. *J Biol Chem* 1994;269:30994–8. https://doi.org/10.1016/S0021-9258(18)47380-2
50. Ghosh A, Pandey SP, Joshi DC *et al.* Identification of G-quadruplex structures in MALAT1 lncRNA that interact with nucleolin and nucleophosmin. *Nucleic Acids Res* 2023;51:9415–31. https://doi.org/10.1093/nar/gkad639
51. Bañuelos S, Lectez B, Taneva SG *et al.* Recognition of intermolecular G-quadruplexes by full length nucleophosmin. Effect of a leukaemia-associated mutation. *FEBS Lett* 2013;587:2254–9.https://doi.org/10.1016/j.febslet.2013.05.055
52. Phan AT, Kuryavyi V, Gaw HY *et al.* Small-molecule interaction with a five-guanine-tract G-quadruplex structure from the human MYC promoter. *Nat Chem Biol* 2005;1:167–73. https://doi.org/10.1038/nchembio723
53. Arimura Y, Konishi HA, Funabiki H. MagIC-Cryo-EM: structural determination on magnetic beads for scarce macromolecules in heterogeneous samples. *eLife* 2024;13:RP103486. https://doi.org/10.7554/eLife.103486
54. Warren C, Matsui T, Karp JM *et al.* Dynamic intramolecular regulation of the histone chaperone nucleoplasmin controls histone binding and release. *Nat Commun* 2017;8:2215. https://doi.org/10.1038/s41467-017-02308-3
55. Onikubo T, Nicklay JJ, Xing L *et al.* Developmentally regulated post-translational modification of nucleoplasmin controls histone sequestration and deposition. *Cell Rep* 2015;10:1735–48. https://doi.org/10.1016/j.celrep.2015.02.038
56. Mitrea DM, Cika JA, Stanley CB *et al.* Self-interaction of NPM1 modulates multiple mechanisms of liquid–liquid phase separation. *Nat Commun* 2018;9:842. https://doi.org/10.1038/s41467-018-03255-3
57. Shimamura H, Yamazaki H, Yoshimura SH. Charge block-driven liquid–liquid phase separation: a mechanism of how phosphorylation regulates phase behavior of disordered proteins. *Biophys Physicobiol* 2024;21:e210012. https://doi.org/10.2142/biophysico.bppb-v21.0012
58. Federici L, Falini B. Nucleophosmin mutations in acute myeloid leukemia: a tale of protein unfolding and mislocalization. *Protein Sci* 2013;22:545–56. https://doi.org/10.1002/pro.2240
59. Urbaneja MA, Skjærven L, Aubi O *et al.* Conformational stabilization as a strategy to prevent nucleophosmin mislocalization in leukemia. *Sci Rep* 2017;7:13959. https://doi.org/10.1038/s41598-017-14497-4
60. Timr S, Sterpone F. Computational insights into the unfolding of a destabilized superoxide dismutase 1 mutant. *Biology* 2021;10:1240. https://doi.org/10.3390/biology10121240
61. Chiarella S, De Cola A, Scaglione GL *et al.* Nucleophosmin mutations alter its nucleolar localization by impairing G-quadruplex binding at ribosomal DNA. *Nucleic Acids Res* 2013;41:3228–39. https://doi.org/10.1093/nar/gkt001
62. Mitrea DM, Grace CR, Buljan M *et al.* Structural polymorphism in the N-terminal oligomerization domain of NPM1. *Proc Natl Acad Sci USA* 2014;111:4466–71. https://doi.org/10.1073/pnas.1321007111
63. Arcovito A, Chiarella S, Della Longa S *et al.* Synergic role of nucleophosmin three-helix bundle and a flanking unstructured tail in the interaction with G-quadruplex DNA. *J Biol Chem* 2014;289:21230–41. https://doi.org/10.1074/jbc.M114.565010
64. Mitrea DM, Cika JA, Guy CS *et al.* Nucleophosmin integrates within the nucleolus via multi-modal interactions with proteins displaying R-rich linear motifs and rRNA. *eLife* 2016;5:e13571. https://doi.org/10.7554/eLife.13571
65. Okuwaki M, Ozawa S-I, Ebine S *et al.* The stability of NPM1 oligomers regulated by acidic disordered regions controls the quality of liquid droplets. *J Biochem* 2023;174:461–76. https://doi.org/10.1093/jb/mvad061

Received: July 23, 2025. **Revised:** January 12, 2026. **Accepted:** January 23, 2026